



Published in final edited form as:

Pharm Res. 2015 October ; 32(10): 3170–3187. doi:10.1007/s11095-015-1695-1.

Validating CFD Predictions of Pharmaceutical Aerosol Deposition with *In Vivo* Data

Geng Tian¹, Michael Hindle², Sau Lee³, and P. Worth Longest^{1,2,*}

¹Department of Mechanical and Nuclear Engineering, Virginia Commonwealth University, Richmond, VA

²Department of Pharmaceutics, Virginia Commonwealth University, Richmond, VA

³Office of Pharmaceutical Science, United States Food and Drug Administration

Abstract

Purpose—CFD provides a powerful approach to evaluate the deposition of pharmaceutical aerosols; however, previous studies have not compared CFD results of deposition throughout the lungs with *in vivo* data.

Methods—The *in vivo* datasets selected for comparison with CFD predictions included fast and slow clearance of monodisperse aerosols as well as 2D gamma scintigraphy measurements for a dry powder inhaler (DPI) and softmist inhaler (SMI). The CFD model included the inhaler, a characteristic model of the mouth-throat (MT) and upper tracheobronchial (TB) airways, stochastic individual pathways (SIPs) representing the remaining TB region, and recent CFD-based correlations to predict pharmaceutical aerosol deposition in the alveolar airways.

Results—For the monodisperse aerosol, CFD predictions of total lung deposition agreed with *in vivo* data providing a percent relative error of 6% averaged across aerosol sizes of 1–7 μm . With the DPI and SMI, deposition was evaluated in the MT, central airways (bifurcations B1–B7), and intermediate plus peripheral airways (B8 through alveoli). Across these regions, CFD predictions produced an average relative error <10% for each inhaler.

Conclusions—CFD simulations with the SIP modeling approach were shown to accurately predict regional deposition throughout the lungs for multiple aerosol types and different *in vivo* assessment methods.

Keywords

Computational fluid dynamics (CFD); predictions of aerosol deposition; airway dosimetry predictions; pharmaceutical aerosols; respiratory drug delivery

INTRODUCTION

The efficacy of inhaled pharmaceutical aerosols often depends on their deposition location within the airways (1). For example, inhaled medication that deposits in the oropharynx does

***Author Contact Information:** Dr. P. Worth Longest, PhD (Corresponding author), Virginia Commonwealth University, 401 West Main Street, P.O. Box 843015, Richmond, VA 23284-3015, Phone: (804)-827-7023, Fax: (804)-827-7030, pwstringest@vcu.edu.

not contribute to improving lung function and, when swallowed, is often associated with adverse side effects. Within the lungs, the deposition site of inhaled medications is also a significant factor in efficacy. Inhaled surfactants must be deposited in the alveolar region to have an impact on reducing the work of lung inflation and breathing (2). Inhaled antibiotics should be delivered to the site of infection at sufficient concentrations to kill the underlying bacteria, otherwise microorganism resistance to the antibiotic can occur (3). Asthma therapy is often envisioned as being most effective when delivered to the upper airways (4). However, significant evidence indicates that both the large and small airways experience inflammation with asthma as well as COPD (5, 6). In fact, the small airways display a higher degree of inflammation in pediatric asthma compared with adults (7). Predicting the site of pharmaceutical aerosol deposition within the airways is important to both understand and improve the efficacy of inhaled medications. Computational fluid dynamics (CFD) models provide an effective approach to simulating pharmaceutical aerosol delivery from the site of aerosol formation in the inhaler to deposition throughout the lungs.

Simulating the deposition of pharmaceutical aerosols in the lungs was recently reviewed by Longest and Holbrook (8). Airway dosimetry models can be classified as semi-empirical, whole-lung 1D (one-dimensional), and CFD 3D (three-dimensional). Semi-empirical models provide correlations for whole-lung deposition or regional deposition based on fitting empirical data as a function of analytical parameters (9). Finlay and Martin (10) recently reviewed historical semi-empirical models and new developments in predicting aerosol deposition in the respiratory tract. The whole-lung semi-empirical model developed by Martin and Finlay (11) was shown to match whole-lung *in vivo* deposition for ambient aerosols to a high degree. Additional corrections are required to account for jet effects associated with inhaler mouthpieces (12). Whole-lung 1D models assume either a single path (13) or stochastic (14) lung geometry and employ algebraic expressions for aerosol deposition by different physical mechanisms such as sedimentation, impaction, and diffusion (15). For nebulized and ambient particles, these models often match available *in vivo* data in terms of total TB and alveolar deposition (16) relatively well. As a recent example of a whole-lung 1D model, the study of Katz et al. (17) compared model predictions to a newly developed high resolution *in vivo* lung deposition dataset (18) and found limitations in the model's predictive ability to capture mouth-throat (MT) deposition and to resolve deposition within the tracheobronchial (TB) region. Predictions in the alveolar region and exhaled mass fraction are also frequently inaccurate (16, 19, 20). While efficient, the primary limitation of semi-empirical and 1D whole-lung approaches is the exclusion of a number of factors that contribute to the deposition of pharmaceutical aerosols. Some of these excluded factors are jet and spray momentum associated with inhaler use (21), hygroscopic and evaporative effects resulting in size change of droplets (22), turbulence (23), bifurcating geometries (24), and realistic alveolar models (25). The semi-empirical and 1D approaches can be extended to account for these factors; however, this is often difficult and may rely on correlations developed from CFD simulations (26) or *in vitro* experiments (27).

CFD models of pharmaceutical aerosols have a number of advantages compared with semi-empirical and 1D whole-lung approaches. CFD simulations are based on solution of the

underlying transport equations, which can directly account for factors such as transient flow, turbulence and turbulent particle dispersion, hygroscopic particle size change, and fluid-wall interactions in complex geometries. With CFD simulations realistic geometries are employed, which are necessary to account for deposition in complex structures like the larynx (28), bifurcations, and constricted airways (29). Highly realistic models of the alveolar region including wall motion are also possible (30). Considering pharmaceutical aerosols, CFD simulations can directly predict the effects of jet and spray momentum from an inhaler on an aerosol as it enters the MT and upper TB airways (21). Limitations of CFD models include complexity in capturing the physics associated with pharmaceutical aerosol generation and delivery, difficulty in resolving flow dynamics in the vast expanse of the bifurcating airways, and computational expense. As a result, CFD models are typically limited to sections of the respiratory tract (31-35), such as from the oral cavity as far as approximately the sixth bifurcation (31), or employ simplifications to predict deposition throughout the TB airways.

Only recently have several new modeling techniques made CFD simulations of aerosols over broad ranges of the lungs possible (36-39). Lin et al. (36) proposed a combination of 3D CFD simulations to resolve transport and deposition in the upper airways together with 1D semi-empirical modeling in the deeper lung. Kleinstreuer and Zhang (39) developed a triple bifurcation unit that was repeated in parallel and in series to capture deposition efficiency throughout the TB region. Using a different approach, Longest and co-workers (23, 40, 41) have developed the stochastic individual pathway (SIP) model in which individual continuous pathways beyond the third bifurcation (B3) are generated extending into each lobe of the lung through the terminal bronchioles (B15). Along each pathway, one daughter branch of each bifurcation is continued and one is not, which is similar to the 1D whole lung Monte Carlo modeling technique of Koblinger and Hofmann (16). A sufficient number of stochastically generated pathways are simulated until deposition results converge to an ensemble average (40). This approach is reported to reduce the required time to simulate the full TB region by a factor of 3×10^5 with only an estimated minor loss in accuracy (40). Additional simplifications allowing for the use of monodisperse aerosols and steady state simulations beyond B3 provide further time savings and retain high accuracy (23). Recently, CFD was also implemented to determine total particle deposition in acinar geometries extending from the terminal bronchioles resulting in correlations to predict alveolar deposition as a function of aerosol size and residence time for breathing profiles consistent with inhaler use (42). The combination of the SIP approach together with the new CFD-derived alveolar deposition correlations results in a method for CFD-based predictions of pharmaceutical aerosol deposition throughout the airways.

Applications of the SIP modeling approach applied to pharmaceutical aerosols thus far have been the evaluation of existing inhalers (23, 40, 41) and the development of new respiratory drug delivery strategies (43-45). For example, a CFD-based comparison of a widely prescribed metered dose inhaler (MDI) and dry powder inhaler (DPI) revealed that the MDI delivered approximately twice the dose to the TB region for both correct usage and with one form of common usage error (41). Both inhalers delivered very little drug (<1% of the nominal dose) to the important lower (or small) TB airways (41). A CFD model investigation using the SIP approach of the Respimat inhaler (Boehringer Ingelheim,

Ingelheim, Germany) indicated that it could increase delivery efficiency to the small TB airways by over an order of magnitude compared with a conventional DPI (23). Furthermore, CFD whole-lung simulations have been employed for the development of excipient enhanced growth (EEG) aerosol delivery and revealed negligible MT deposition combined with the potential for even higher doses to the small airways or high alveolar dose, depending on the intended airway target (44). These CFD predictions have been extensively validated with comparisons of drug deposition to *in vitro* datasets in the upper airways through approximately the third respiratory bifurcation using identical inhalers and geometries in the models and experiments (23, 40, 41, 44, 46). Moreover, extensive work has been performed to validate CFD model predictions in bifurcating geometries of lower TB airways (28, 47-49). However, comparisons of CFD-based whole-lung deposition data with *in vivo* results for pharmaceutical aerosols have previously not been reported.

The objective of this study is to validate regional CFD predictions of pharmaceutical aerosol deposition throughout the lungs by direct comparisons to multiple *in vivo* datasets. Multiple techniques are available for predicting and reporting *in vivo* aerosol deposition (50). In this study, selected *in vivo* datasets include the fast and slow clearance data reported by Stahlhofen et al. (9) for ambient aerosols, 2D gamma scintigraphy for the budelin Novolizer DPI (Meda Pharmaceuticals, Somerset, NJ, USA) based on Newman et al. (51), and 2D gamma scintigraphy for the fenoterol Respimat soft mist inhaler (SMI) based on Newman et al. (52). While not exhaustive, this *in vivo* data selection provides a broad range of aerosol types (monodisperse, dry powder, spray) combined with the two most developed methods for *in vivo* aerosol reporting evaluated in healthy adults. The selected lung geometry for CFD simulations is a previously developed characteristic model intended to represent deposition for average-size adults (53, 54). Comparisons are made between CFD predictions and *in vivo* data on the basis of regional deposition in the MT, TB airways (including lung central and peripheral sections) and alveolar region. To facilitate the CFD simulations, *in vitro* testing of aerosol size was conducted to accurately determine the initial polydisperse size distribution entering the MT. Agreement between the CFD predictions and *in vivo* datasets within the regions considered will provide confirmation that the CFD predictions are highly accurate throughout the lungs.

MATERIALS AND METHODS

Selection of *In Vivo* Datasets

In vivo datasets of aerosol deposition were selected to capture a range of aerosol complexity and provide information on regional aerosol deposition throughout the airways of healthy adults. The *in vivo* lung deposition data reported by Stahlhofen et al. (9) was selected first as a case with a simple monodisperse aerosol and controlled breathing parameters. In the studies reported by Stahlhofen et al. (9), lung deposition was assessed by labeling the aerosol with a radiotracer and imaging total lung deposition followed by imaging the fraction remaining in the airways after 24 hours. The resulting fast and slow clearance fractions of deposited aerosol are associated with initial tracheobronchial (TB) and alveolar deposition, respectively. However, previous studies have reported significant fractions of particles depositing in the TB airways which clear slowly and are not captured by 24-hour

clearance estimates (55). In the studies reported by Stahlhofen et al. (9), breathing parameters were carefully controlled and a large mouthpiece was implemented, resulting in an open mouth position. Finally, the simple monodisperse aerosols employed were composed of stable materials that did not change size in the airways. The specific dataset selected for comparison to CFD predictions in this study employed a 30 L/min (LPM) inhalation flowrate with a 4 s breathing period (2 s inhalation) and a 1 L tidal volume, which was originally considered by Heyder et al. (56) and included in the broader analysis of Stahlhofen et al. (9).

For a first representative pharmaceutical aerosol, the *in vivo* study of Newman et al. (51) was selected, which considers a Novolizer DPI (Meda, Pharmaceuticals, Somerset, NJ) with a formulation containing a 200 µg dose of budesonide combined with a lactose carrier. The Novolizer device has a relatively small outlet orifice with a 6 mm diameter, which creates a high speed jet of air in the oropharynx with elevated turbulence and aerosol deposition. In the study of Newman et al. (51), the budesonide powder was radiolabeled and the subjects inhaled at characteristic (measured) peak inspiratory flow rates (PIFR) of 54, 65, or 99 LPM. Two dimensional (2D) gamma scintigraphy images (coronal plane) of the lung were then taken to map aerosol deposition to the central, intermediate, or peripheral lung regions (57). In these experiments, depositions in the trachea and esophagus were combined with MT dose estimates. The central lung region was defined as 20% of the area of the entire lung boundary. For comparisons to CFD estimates in this study, the case of *in vivo* lung deposition with the highest peak inspiratory flow rate (PIFR) of 99 LPM is considered, which is the most consistent with the intended operating flow rate of the Novolizer DPI at a standard 4 kPa pressure drop.

As a second pharmaceutical aerosol, the study of Newman et al. (52) was considered, which evaluated the Respimat softmist inhaler (SMI; Boehringer Ingelheim, Ingelheim Germany) with an aqueous formulation of fenoterol. The drug was radiolabeled and delivered to subjects using either the Respimat inhaler or a metered dose inhaler (MDI) with or without a spacer. Subjects were instructed to inhale slowly and deeply with a target flow rate of approximately 30 LPM followed by a 10 s breath-hold. The Respimat was fired after inhalation began and the Respimat inhaler is known to generate an aerosol for a period of approximately 1.5 s (22). 2D gamma scintigraphy images of the device and airways were then captured with a gamma camera and subdivided into central, intermediate, and peripheral lung regions using the standard technique of Newman's group (57). As with the DPI study, deposition in the trachea and esophagus was added to MT deposition. Size distribution of the Respimat aerosol with fenoterol based on estimates from a multistage liquid impinger were also available (58). The Respimat aerosol has previously been shown to have considerably less spray momentum than a MDI or DPI (22, 59). However, the mouthpiece shape is known to influence deposition in the device and possibly the MT (22). Previous studies have predicted a relatively small effect of droplet evaporation on the device and MT deposition for the Respimat aerosol (22). In deeper lung regions, evaporation of the aerosol is limited due to high relative humidity (43).

Inhalers and Inhalation Waveforms

The Novolizer device was previously described in the study of Fenton et al. (60). With this DPI, the drug (budesonide) is stored in the device as a powder that is blended with much larger (approximately 50 μm) lactose carrier particles. The Novolizer forms an aerosol by passing air over a metered mass of powder (drug and carrier), with the initially formed aerosol passing through a cyclone impactor and then exiting the inhaler through a 6 mm diameter jet. The jet is located in the middle of an oval 20 \times 25 mm mouthpiece, which serves to maintain an open mouth position when using the inhaler. Delvadia et al. (54) recently considered the same budesonide Novolizer, and evaluated MT, upper TB and lung delivery with *in vitro* experiments using a replica airway geometry very similar to the one implemented in the current study. Delvadia et al. (54) showed that *in vitro* deposition characteristics in the MT and lung were very similar to the *in vivo* data reported by Newman et al. (51) and scaling of the MT-TB model could account for intersubject variability.

For comparison with the *in vivo* study of Newman et al. (52), the Respimat softmist inhaler (SMI) was considered, which was previously described in the studies of Dalby et al. (61) and Longest and Hindle (22). This device forms an aerosol by colliding two microscale streams of liquid drug solution at a predetermined angle (approximately 90°), which creates breakup of the liquid columns and a spray effect. The device typically delivers 15 μL of solution over a period of 1.5 s, which is considerably longer than with MDI spray devices (~0.2 s) (62). Previous studies have reported the MT and induction port deposition characteristics of the Respimat based on *in vitro* experiments (22, 63), *in vivo* experiments (52, 64), and CFD modeling (22, 63). The mouthpiece of the inhaler contains side inlet vents through which the inhaled air passes. A central post within the mouthpiece contains the collision nozzle for forming the aerosol. Longest and Hindle (22) previously showed that recirculating airflow in front of the central post (in the region of aerosol formation) was partially responsible for device drug deposition.

Considering the inhalation experiments of Stahlhofen et al. (9), breathing was characterized by an inhalation flow rate of 30 LPM, breathing period of 4 s (2 s inhalation) and inhaled volume of 1 L. To approximate the quiescent breathing profile of the subjects in the Stahlhofen et al. (9) study, a sinusoidal inhalation waveform was employed, which is illustrated in Figure 1 and described in Table 1.

Effective use of DPIs typically requires quick-and-deep (QD) inhalation whereas SMIs are intended to be used with slow-and-deep (SD) inhalation. Characteristic inhalation waveforms for both QD and SD inhalation were previously developed and reported by Longest et al. (41) based on comparisons to multiple *in vivo* studies. For the Novolizer DPI, the characteristic QD inhalation profile was considered with critical values of peak inspiratory flow rate (PIFR) = 99 LPM and inhaled volume equal to 3 L, based on measurements from the *in vivo* deposition study of Newman et al. (51). The resulting QD inhalation waveform is quantified in Table 1 and illustrated in Fig. 1 with a mean inhalation flow rate of 60.8 LPM. Similarly for the SMI, the targeted inhalation flow rate of 24.8 LPM and inhaled volume of 3 L produced a SD waveform that is described in Table 1 and Fig. 1.

Airway Models

The inhalers were connected to a characteristic MT geometry based on the elliptical model originally proposed by Xi and Longest (65) (Fig. 2). This MT model was developed from the oral airway cast reported by Cheng et al. (66) and in-house CT data of the pharynx and larynx. The original inlet diameter of the MT model was 22 mm, which was considered similar to the top-to-bottom mouthpiece diameters of both inhalers. As a result, changes to the oral airway volume were not implemented to account for changes in the jaw position. The inhalers were directly connected to the MT geometry assuming an insertion depth of 0.5 cm and an angle of zero degrees with the horizontal plane (59). This insertion depth creates a small difference from the previous *in vitro* and numerical studies of Delvadia et al. (54) and Longest and Hindle (22). However, mouthpiece insertion only accounts for a small portion of the oral cavity length with these inhalers and is expected to have a very minor effect on the results. The studies of Delvadia et al. (54, 67) previously reported that this MT model was similar in dimensions to values of the mean adult population and, when used for *in vitro* studies, produced DPI deposition values consistent with averages from multiple *in vivo* experiments.

The whole-lung CFD model includes a complete geometry of the upper airways from the trachea through approximately the third respiratory bifurcation (B3; Fig. 2). The upper TB airway geometry selected was Model C described by Walenga et al. (53), which was based on the anatomical cast dimensions reported by Yeh and Schum (68) and scaled to a functional residual capacity (FRC) of 3.5 L to represent an adult male (69). Walenga et al. (53) demonstrated that this model provided airway dimensions consistent with mean values for an adult population. Anatomical features included in Model C are cartilaginous rings in the trachea, a D-shaped tracheal cross-section, asymmetrical bifurcations, and out-of-plane rotation of the bifurcations, all consistent with the Yeh and Schum (68) data. Features not included in this model, but explored by Walenga et al. (53), include curvature of the main bronchi, non-circular cross-sections beyond the trachea, and non-ideal bifurcation shapes. The selection of the Yeh and Schum (68) airway anatomy was based on the fact that it provides separate sets of airway dimensions for each of the five lung lobes. Differences among existing airway geometries have previously been characterized (70). For comparisons between regional *in vivo* deposition data and CFD predictions, Model C is expected to provide an adequate degree of anatomical detail. The validation of this assumption will be assessed in the Results section.

Beyond the third bifurcation, stochastic individual path (SIP) models were considered extending into each of the five lung lobes (Fig. 2). Bifurcations within the SIP models were constructed as physiologically realistic bifurcation units (71) with the airway dimensions reported by Yeh and Schum (68), again scaled to a FRC of 3.5 L. An advantage of the Yeh and Schum (68) data is that average dimensions are provided for each lung lobe. Use of the individual path model based on defined bifurcating units allows for the application of a hexahedral mesh, which improves solution accuracy, computation speed, and requires fewer cells to adequately resolve the flow domain (72). Continuation of the left or right branch of each bifurcation was considered to be consistent with the flow distribution, resulting in an equal probability for the symmetric outflow assumption. However, if a selection at each

bifurcation led out of the general region of a specific lung lobe, the SIP generation process was restarted. General lung lobe regions were estimated from in-house CT scans. Consecutive branches were rotated at 90° to approximate physiological conditions (73). Bifurcation 15 (B15) was assumed to end with the terminal bronchioles in each lobe, based on existing anatomical data (68). From the previous study of Longest et al. (23), deposition in the left lower (LL) lobe provides a characteristic average of deposition in all five lung lobes. As a result, this approximation was implemented in the simulations and was also evaluated further in the current study.

Previous modeling approaches to simulate alveolar deposition of pharmaceutical aerosols have relied on empirically based estimates from *in vivo* studies (9) or analytically-based estimates that employ particle deposition mechanisms. The empirically-based estimates do not include breathing profiles used with pharmaceutical aerosols (e.g., QD or SD inhalation with breath-hold), whereas the analytically-based estimates neglect an accurate alveolar structure. To improve the accuracy of predicted pharmaceutical aerosol deposition in the alveolar region, Khajeh-Hosseini-Dalasm and Longest (42) recently developed an approximate CFD model of the entire acinar region (Fig. 3). In this previous study, it was determined that a multigenerational approximation of the acinar region could be used to predict deposition within the total region distal to a terminal bronchiole. CFD simulations were then used to develop correlations for alveolar deposition considering a range of particle sizes and pharmaceutical inhalation waveforms consistent with SD and QD inhalation as well as a breath-hold period. These SD and QD correlations (42) were judged to be adequate approximations of the waveforms implemented in the current study and were therefore used to make CFD-based estimates of deposition in the alveolar region for the DPI and SMI. As with other aspects of the whole-lung CFD model, anatomical dimensions of the alveolar region are consistent with an average adult.

CFD Simulations

Based on previous CFD simulations with inhalers (22, 41), turbulent flow is expected in the MT region and upper TB airways, which is enhanced by the air jets issuing from the DPI (59) and the glottis (28). Transition from turbulent to laminar flow occurs in the upper TB airways through approximately bifurcation B4. Turbulence can be simulated in the region of B4-B7, but it is questionable if turbulence is sufficient in this region to affect particle deposition. In regions where turbulent flow is expected, the LRN $k-\omega$ model was selected based on its ability to effectively and accurately predict pressure drop, velocity profiles, and shear stress for transitional and turbulent flows (74, 75). Another significant advantage of the LRN $k-\omega$ model is numerical efficiency, which allows for the simulation of typical SMI spray times (e.g., 1.5 s) and transient inhalation profiles (Table 1). The conservation of mass and momentum equations used with the LRN $k-\omega$ model are available from Wilcox (75) and were previously reported by Longest and Xi (76). Similarly, the equations governing turbulent kinetic energy (k) and specific dissipation rate (ω) were also reported by Longest and Xi (76). The LRN $k-\omega$ model resolves the flow field through the buffer and viscous sub-layers in transitional and turbulent boundary layer and internal flows (75), provided that the near-wall mesh spacing is sufficient. In lower airway regions such as B8-B15 and the alveolar region, turbulence does not occur and laminar simulations were conducted.

Based on the aerosol size experiments, the polydisperse size distributions include particles ranging from the submicrometer scale to greater than 10 μm . To address this broad range of particle sizes, a previously developed and optimized Lagrangian particle tracking method was employed (77, 78). The gravity vector was oriented to represent subjects sitting or standing while inhaling the aerosol, which is consistent with the three *in vivo* studies selected for comparison to the CFD predictions.

To model the effects of turbulent fluctuations on particle trajectories, a random walk method was implemented (79). The primary limitation of this eddy interaction model in conjunction with the Reynolds Averaged Navier Stokes equations is that it does not account for reduced turbulent fluctuations in the wall-normal direction, which results in an over-prediction of deposition (80). To better approximate turbulent effects on particle deposition, an anisotropic turbulence correction was applied for particle tracking (80, 81). In this study, the exponential wall-normal damping function f_n was evaluated for n^+ values ranging from 0 to a maximum of 60.

Based on the results of Tian et al. (40), transient simulations are required in the upper airways through approximately B3, whereas steady state approximations are acceptable in the SIP models. In this study, transient simulations are conducted for the inhalers, MT and upper TB airways for the complete sinusoidal, QD, and SD inhalation waveforms. For the individual SIP models, steady state simulations are then performed at the equivalent mean flow rates (Table 1). In these steady state simulations, the inhalers and upper MT-TB models are included to generate approximate flow fields and particle conditions at the inlet to each of the SIP geometries. Tian et al. (40) showed that this approach was accurate to within 5% of fully transient simulations in both the upper and lower airways, and provided a significant savings in solution time.

In performing the CFD simulations, previously established best-practices were implemented to provide a high quality solution. For the MT-TB model, including one SIP geometry, grid convergent results were found to occur with meshes consisting of approximately 1.8 million control volumes. Specifically, coarse, medium, and fine grids of approximately 850,000, 1,250,000 and 1,800,000 control volumes were considered. Maximum velocity values and deposition fractions varied by less than 2% between the 2 highest grid densities considered. As a result, the fine grid was implemented in this study. To improve the accuracy of particle deposition predictions in the turbulent flow fields, near-wall interpolation of the velocity profile was included, as described by Longest and Xi (78). Both near-wall anisotropic turbulence corrections and near-wall velocity interpolation were included with user-defined functions.

In order to produce deposition results that were independent of the number of particles simulated, two types of particle distribution profiles (monodisperse vs. polydisperse) were considered. For the monodisperse assumption, approximately 90k particles at the aerosol inlet of the Novolizer and Respimat were required to produce convergent deposition results. For the Novolizer with a polydisperse aerosol, nine size bins consistent with the midpoint cut-off sizes of the Next Generation Impactor (NGI) stages implemented at a flow rate of 80 LPM were considered. Similarly for the Respimat inhaler, size bins were defined consistent

with the experimental particle size determination using the multistage liquid impinger from Steed et al. (58). To resolve deposition for all of the size bins for either inhaler, 450k particles were considered at the inlet of each model section. These values were determined as the number of required particles to reduce change in regional deposition fractions to below 5% relative difference with the addition of 10k monodisperse particles and 50k polydisperse particles.

Particle release timing was defined to match the *in vivo* experimental conditions as closely as possible. For the monodisperse case of Stahlhofen et al. (9), particles were released over the first 1 s of the sinusoidal inhalation waveform in order to approximate buildup and release of the nebulized aerosol, which was continuously produced in the *in vivo* experiments. With the Novolizer DPI, particle release timing was defined as 0-0.5 s of the QD inhalation waveform, which is consistent with expected emptying of the DPI. For the Respimat inhaler, aerosols were released during the 0-1.5 s period of the SD waveform, which is the previously reported spray time of this device (62).

SIP Model Considerations

To implement the SIP model approach, multiple factors need to be considered including division of the geometry into sections, interpolation of velocity and particle profiles between sections, use of transient or steady state simulations, use of monodisperse or polydisperse aerosols, and selection of outlet boundary conditions. To facilitate the CFD solution, the model was divided into three sections, which were the inhaler to B3 (including the complete asymmetrical upper TB region), B4-B7 (middle TB airways), and B8-B15 (lower TB airways). Division of the model into multiple sections may not be necessary; however, this division helps to match flow physics in each section with an appropriate CFD model and reduces the number of particle trajectories required in the upper model regions. Based on previous studies, transport into the LL lobe was used as a representative average value of conditions in the five lung lobes. Transient simulations were implemented for the inhaler and upper airways through B3, whereas simulations in the SIP geometries implemented steady state conditions with velocity profiles interpolated at mean flow conditions. Particles were initialized at inlets of B4 and B8 using the polydisperse size distribution from the outlet of the respective upstream branches and using either a blunt or parabolic spatial profile, respectively. Polydisperse size distributions were implemented in all simulations except one case where the effect of assuming a monodisperse profile with a size equal to the polydisperse MMAD \times 1.25 was tested in the SIP geometry, based on the findings of Longest et al. (23).

Outflow boundary conditions in the upper TB model were based on estimates of ventilation to each lung lobe. Lobar ventilation approximations presented in the studies of Horsfield et al. (82), Asgharian and Price (83), and Yin et al. (84) were considered. Reasonable consistency among these studies led to the following distribution estimates for each of the five lung lobes: right upper 14%, right middle 7%, right lower 33%, left upper 15%, left lower 31%. The resulting right and left ventilation proportions were 54 and 46%, respectively. Beyond the lobar bronchi, symmetric outflow conditions were assumed at each bifurcation level (B4-B15), in which equal mass flow rates exit each branch, consistent with

the assumption of equal downstream subtended volume within each lobe. This assumption is not expected to largely influence the regional and local deposition characteristics of interest in this study.

Determination of Initial Aerosol Size Distributions

Accurate estimates of the aerosol sizes implemented in the three selected *in vivo* experiments are required for reliable comparisons of the *in vivo* lung deposition data and CFD estimates. For the monodisperse aerosol experiments reported by Stahlhofen et al. (9), lung deposition data is reported in terms of aerodynamic diameters, which were directly implemented in the corresponding CFD calculations. Considering the Respimat inhaler with an aqueous fenoterol formulation, the *in vivo* study of Newman et al. (52) refers to a previous *in vitro* study where the polydisperse size distribution of this inhaler and formulation combination was measured (58). These size measurements, reported by Steed et al. (58), were implemented to define the Respimat particle size distribution (PSD) using the midpoint size of each stage of the multistage liquid impinger operated at 60 LPM.

For the Novolizer, the inhalation flow rate is known to influence particle size distribution exiting the inhaler. As a result, new experimental measurements considering the selected QD waveform were needed. Aerosol size measurement during a constant inhalation flow rate was needed based on the requirement of constant flow through the impactor. However, it is expected that implementing the mean flow rate underestimates conditions occurring when a majority of the powder exits the Novolizer device. As a result, the inhaler was tested at a constant flow rate equal to the average of the mean and PIFR, or 80 LPM.

For sizing the Novolizer DPI aerosol, a Next Generation Impactor (NGI; MSP Corp., Shoreview, MN) was operated at a constant flow rate of 80 L/min, which is consistent with the QD inhalation waveform as described above. The Novolizer DPI was connected directly to a preseparator using a mouthpiece adaptor to ensure an airtight seal and the flow was generated using a vacuum pump. A three-way solenoid valve downstream of the impactor was used to generate a square wave inhalation waveform of 80 L/min for 3 s to actuate the DPI and draw a total 4 L of air through the system, based on standard DPI aerosol characterization protocols. Impactor stages and the preseparator were coated to prevent particle bounce and re-entrainment. Drug deposition in the impactor was determined using a validated HPLC assay method for budesonide for four single dose experiments. Particle size distributions were reported as budesonide mass distribution recovered from the impactor. The mass median aerodynamic diameter (MMAD) was defined as the particle size at the 50th percentile on a cumulative percent mass undersize distribution (D50) using linear interpolation.

Measured particle size distributions were translated to size bins in the numerical model using the midpoint cut-off diameters of the NGI stages for a flow rate of 80 LPM. Drug mass in the NGI pre-separator was assumed to have the pre-separator cut-off diameter of approximately 11.4 μm . It is expected that a fraction of this aerosol in the pre-separator is composed of larger diameter particles due to the presence of some drug remaining attached to lactose carrier particles. However, this underestimate of their particle size is of little significance, as at these sizes they would all typically be retained in the MT region. As a

result, MT and TB partitioning of drug will be similar to partitioning values that would occur from a more exact fractioning of sizes above 11.4 μm . The quality of this assumption will be evaluated with comparisons between the CFD predictions and *in vivo* estimates of drug deposition for the DPI.

Deposition Fraction Mapping

The calculation of regional deposition fractions (DF) using the SIP whole-lung modeling approach has previously been described (23, 40, 41). For clarity, DF is defined as the mass of drug deposited within a specific region divided by the mass of drug entering the airways (or initially aerosolized). These calculations take into account the mass of drug associated with aerosol particles or droplets of different sizes comprising the polydisperse aerosol size distribution. Further details on calculating DF in the airways using the SIP approach are provided in the studies of Longest et al. (41) and Tian et al. (40).

Using the SIP approach, DF is typically reported regionally for the inhaler, MT, upper TB airways (B1-B3), intermediate TB airways (B4-B7), lower TB airways (B8-B15), and alveolar region. This approach is useful as it matches the typical physiological divisions of lung zones. For example, region B8-B15 and the alveolar region are typically referred to as the small airways (6). In contrast, the limitations of 2D gamma scintigraphy requires mapping the lung regions to a 2D coronal projection. The approach used by Newman's group (57) is to define the lung boundaries and establish total lung deposition (excluding the trachea). Central deposition is then defined as deposition within a 20% area that is centrally located within each lung.

For the comparison of 3D CFD predictions of regional deposition with the 2D gamma scintigraphy studies of Newman et al. (51, 52), a conversion or mapping technique of the CFD predictions was necessary. To accomplish this mapping, the 3D lung deposition predictions were forward projected onto a coronal plane representing the image that would arise from 2D gamma scintigraphy. The approach used by Newman's group (51, 52) for the validation cases selected in this study was then applied to the 2D projected results to identify the central and peripheral lung regions. Specifically, the extent of the lung boundary was selected using anatomical landmarks and then a 20% area box was positioned within each lung to identify the central region. An illustration of the 2D mapping and region selection is shown in Figure 2. On average, the central (C) region extends to approximately B7 of the SIP geometries based on Figure 2. The intermediate (I) and peripheral (P) regions combined are then B8-B15 and the alveolar region. The adequacy of this mapping approximation is assessed through comparisons of the *in vivo* and CFD deposition data. Based on imperfections with this translational approach, identifying a separate I region is not attempted.

It is important to point out that differences in regional lung definitions can have a large effect on predicted deposition estimates (50); therefore, the approach used in mapping the 3D CFD predictions matched the preexisting selected case studies as closely as possible. New uniform guidelines (85) for estimating lung regions are now different (e.g., 25% vs. 20% central area) from those implemented in Newman et al. (51, 52).

As described above, DF in the alveolar region is estimated based on the correlations developed in the recent study of Khajeh-Hosseini-Dalasm and Longest (42), which account for alveolar particle residence time, aerosol size, as well as QD and SD inhalations, followed by a 10 s breath hold.

RESULTS

Determination of Initial Aerosol Size

Based on cascade impaction in the NGI, the measured mass fraction vs. stage midpoint diameters for the budesonide Novolizer aerosol is reported in Fig. 4 and compared with the measurements of Steed et al. (58) for the Respimat aerosol with a fenoterol formulation. For the budesonide Novolizer combination, the resulting aerosol MMAD (standard deviation; SD) was 2.17 (0.1) μm excluding the fraction depositing in the pre-separator. Including the pre-separator mass fraction of approximately 50%, the MMAD (SD) of the aerosol was 11.4 μm (58). For comparison to the Novolizer DPI, the Respimat aerosol size distribution is also displayed in Figure 4 with a MMAD of 4.92 μm including all stages reported by Steed et al. (58).

Comparison with the *In Vivo* Data of Stahlhofen et al. (9)

Comparisons between CFD predictions of lung deposition and the *in vivo* fast and slow clearance fractions reported by Stahlhofen et al. (9) are reported in Figure 5 and Table 2. CFD predictions for total lung deposition and TB deposition (fast clearance) are based on DF fraction estimates as a percentage of particles entering the MT. CFD predictions of alveolar deposition for the prescribed breathing conditions of the sinusoidal waveform are not yet available. As a result, DF in the alveolar region was calculated using the empirical slow clearance correlation of Stahlhofen et al. (9) and combined with CFD predictions of deposition in the TB region for each monodisperse aerosol size to define total lung deposition. Specifically, alveolar deposition was calculated with the deposition efficiency correlation provided by Eq. (22) of Stahlhofen et al. (9) for slow clearance particles. Alveolar aerosol residence time in the correlation was based on a mean time estimated from the CFD simulations. As described in previous studies (40), the deposition efficiency provided by the correlation was converted to deposition fractions based on the aerosol fraction entering the alveolar airways determined from the CFD results. As a first order approximation in this study, aerosol not deposited in the alveolar region was assumed to be exhaled. Inclusion of the Stahlhofen et al. (9) correlation does not help to validate the CFD results, but it does indicate how the conducting airway simulations can be extended to make regional predictions of aerosol deposition throughout the lungs. It is observed that CFD predictions for both total lung and TB deposition agree with the *in vivo* data (Figure 5 and Table 2). Considering the TB deposition comparison, both the CFD predictions and *in vivo* results indicate a reduction in DF at 7 μm due to increasing depositional losses in the MT region (Figure 5). For the smallest particles considered (1 μm), the CFD results over predict DF in the TB region, which could be due to numerical or experimental inaccuracies, as considered in the Discussion. For sizes beyond a 1 μm diameter, the CFD model slightly under predicts TB deposition, which is most likely due to neglecting TB deposition during exhalation in the model. Nevertheless, the agreement appears adequate between the model

predictions and TB dose considered the large number of variables in both the simulations and *in vivo* experiments. Deposition locations of particles across a range of sizes are also reported in Figure 5. Due to a combination of turbulence, transient flow, and the cartilaginous rings, elevated deposition is observed in the trachea. It is noted that this tracheal deposition is not excluded in comparisons with the *in vivo* data as it is with the 2D gamma scintigraphy comparisons. In the upper bifurcations, local particle deposition occurs primarily at the bifurcations. However, an increasing effect of gravity and sedimentation is observed on deposition in the lower TB bifurcations.

Comparison with the 2D Gamma Scintigraphy Data of Newman et al. (51)

For the Novolizer DPI, comparison between the CFD predictions and *in vivo* data of Newman et al. (51) are provided in Figure 6 and Table 3. Overall, agreement between model predictions and *in vivo* data is excellent. Deposition in the mouthpiece (MP) and MT is combined equaling a value of approximately 67% for both the CFD predictions and *in vivo* data (Fig. 6). Deposition in the central region excludes the tracheal DF in the CFD predictions in order to be consistent with the experimental results. Agreements between CFD predictions and *in vivo* results in both the central (C) and intermediate plus peripheral (I+P) regions indicate that the CFD predictions can adequately resolve the *in vivo* regional lung deposition. Moreover, the observed agreement implies that the selected mapping between the 3D CFD results and 2D gamma scintigraphy images is reasonable.

In addition to a comparison with the Newman et al. (51) data, Table 3 also provides CFD prediction values of drug delivery in physiologically significant lung regions for the Novolizer DPI. Total deposition in the trachea to B3 is reported as 2.7%, which is a small fraction of the total central DF of approximately 10%. As a result, excluding the tracheal deposition (which is less than 2.7%) as was done in the experiments and corresponding CFD predictions, does not have a large effect on deposition in the central region. Surprisingly, DPI deposition in the region of B8-B15 is only 1.8%, which is very low considering the large surface area of these small airways. This low deposition fraction is not captured by the experimental approach of 2D gamma scintigraphy and offers a new insight into the amount of drug delivered to this critical lung region by the DPI with QD inhalation based on CFD predictions.

One potential simplification of the CFD simulations is the use of monodisperse aerosols in the SIP geometry. As described in the Methods, the number of particles simulated in each SIP region can be reduced by a factor of approximately 5x using a monodisperse assumption. Previously, Longest et al. (23) reported that implementing a correction factor of 1.25x to the aerosol MMAD allowed for an accurate monodisperse estimate of regional aerosol deposition. Figure 7 considers regional SIP deposition results for the Novolizer DPI aerosol using the PSD compared with the monodisperse approximation using a correction factor of 1.25. The monodisperse estimate reduced DF predictions in the region of B4-B7 by approximately 20% and increased DF predictions in the region of B8-B15 by approximately 30%. Considering comparisons to the *in vivo* data, implementation of the polydisperse aerosol improved the accuracy of the CFD predictions by a small amount. However,

considering total deposition in the combined region of B4-B15, both the polydisperse aerosol and monodisperse approximation result in DF values of approximately 10%.

Comparison with the 2D Gamma Scintigraphy Data of Newman et al. (52)

Comparison of CFD predictions and *in vivo* experimental results for the Respimat SMI with a fenoterol formulation are displayed in Figure 8 and Table 4. Due to a change in the Respimat mouthpiece (MP) design that occurred after the *in vivo* study of Newman et al. (52) and before the currently available commercial product, comparisons of MP deposition between the *in vivo* results and CFD simulations were not attempted. However, previous CFD studies of the Respimat inhaler compared with *in vitro* deposition data in the current MP design showed excellent agreement when employing the same numerical models used in the current study (22). As a result of this change, the CFD estimates of DF in the airways were corrected to account for the depositional loss in the Respimat MP reported in the experiments (21.9% of the aerosolized drug (52)). As with previous studies for the Respimat, agreement in MT deposition between model predictions and experimental results is excellent (Fig. 8). New in this study, excellent agreement is also observed between CFD predictions of C and I+P deposition and the *in vivo* results of Newman et al. (52) for SD inhalation with the Respimat. Table 4 indicates that the Respimat inhaler increases deposition in the region of B8-B15 by a factor of approximately 5x compared with the Novolizer DPI. Implementing the CFD developed correlations for alveolar deposition during SD inhalation, both the Novolizer and Respimat inhalers provide approximately 20% of the aerosolized dose to the alveolar region (Tables 3 and 4).

The previous results implemented the assumption of the LL lobe SIP model providing an adequate average of alveolar deposition in all five lung lobes. This assumption was based on previous results (23) using a DPI and similar QD inhalation waveform. In Figure 9, simulation results are provided for the Respimat with SD inspiration and including SIP models extending into each lung lobe. DF in the central region (B1-B7) decreases slightly (difference of 0.5%) due to the increase of four additional lung lobes. A minor increase (difference of 0.5%) in CFD predictions of I+P deposition is also observed. However, inclusion of SIP models into all five lung lobes is not observed to improve agreement with the *in vivo* results beyond what is achieved with the LL lobe approximation. As a result, the LL lobe approximation provides an adequate average of regional deposition across all five lung lobes when compared with *in vivo* data for the Respimat inhaler with SD inhalation.

DISCUSSION

This study is the first successful comparison of CFD predictions with *in vivo* pharmaceutical aerosol deposition data across all regions of the lungs. Comparisons were based on a range of aerosol types including monodisperse particles inhaled under quiescent conditions as well as dry powder and spray aerosols inhaled with recommended pharmaceutical inhaler breathing waveforms. Regional lung deposition data was based on two commonly implemented *in vivo* imaging techniques. For comparisons to the Stahlhofen et al. (9) data, the computational predictions of TB deposition had an average 6% relative error across a broad range of particle sizes. Considering the DPI deposition fractions averaged across the

different regions considered, the percent relative error of the computational simulations was 9.9% compared with the experimental *in vivo* data. Similarly for the SMI deposition fractions, the average percent relative error of the computational simulations was 8.5% compared with the experimental data. As a result, CFD simulations and the SIP modeling approach appear to provide a successful method for predicting the regional deposition of simple monodisperse particles and complex DPI and SMI aerosols *in vivo*. These findings are impressive considering the complexity of pharmaceutical aerosol generation and delivery, large differences in flow types and scales from the MT through the alveolar region, variations between the DPI and SMI systems, and expected large intersubject variability in terms of anatomy and inhalation technique.

Successful comparisons of model predictions with *in vivo* aerosol deposition has been a long standing goal in both the dosimetry and respiratory drug delivery fields (8). Previous work with pharmaceutical aerosols has recently indicated good agreement between CFD model predictions and *in vitro* deposition in MT models for DPIs (23, 40, 41, 86), MDIs (41), and SMIs (21, 22, 87). In each of these delivery systems it is important to capture the physics of the inhaler device and resulting jet or spray momentum on aerosol deposition in the MT. The studies of Kleinstreuer et al. (88) and Vinchurkar et al. (89) were the first to implement CFD modeling of MDI generated aerosol deposition in the MT and upper airway geometries. The fraction of aerosol remaining at the exit of the upper airways was assigned to lung deposition, which then matched available total lung *in vivo* deposition data. However, CFD has previously not been used to predict delivery of aerosols throughout the lungs with comparisons to relevant regional *in vivo* data. The current study expands these previous upper airway CFD simulations by successfully predicting aerosol deposition throughout the lungs based on comparisons to similar *in vivo* data for pharmaceutical DPI and SMI products.

Researchers have frequently applied 1D whole-lung models to predict aerosol deposition throughout the lungs (8). Comparisons of these 1D whole-lung models with fast and slow clearance data for monodisperse aerosols are generally successful (15, 90, 91). Similarly in the current study, the whole-lung CFD model accurately captured fast and slow clearance *in vivo* data. One reason for the over prediction of deposition at around 1 μm compared with the fast and slow clearance data may be the increasing fraction of small particles that are slowly cleared from the TB airways (55). In contrast with monodisperse particles inhaled under ambient conditions, whole-lung 1D models have been less successful when compared to more realistic pharmaceutical aerosols. For example, Fleming et al. (19), compared results of a whole-lung 1D model with concurrent *in vivo* deposition using a 3D SPECT approach and nebulized aerosols. Predictions of deposition differed from the *in vivo* results by a factor of 2-fold in the alveolar region and fraction exhaled. In a more recent study, Katz et al. (17) compared the whole-lung 1D model of Martonen et al. (15) to newly developed 3D *in vivo* deposition on a patient specific basis for carefully controlled nebulized aerosols (18). For a large and small aerosol size, simulated lung deposition varied from measured lung deposition by a difference of 15-20% (relative difference of 20-30%). These differences were largely due to inaccuracies in the MT and alveolar regions.

In contrast with the whole-lung 1D modeling approach, strengths of the new CFD whole-lung model included improved accuracy in MT deposition that takes into account effects of the inhaler on deposition and improvements in alveolar predictions of deposition. As a result of these improvements, very good agreement is observed between model predictions and *in vivo* results in all regions of the airways. The CFD predictions also allow for direct inclusion of factors such as hygroscopic aerosol size increase (92), moving airway walls (42), and aerosol electrostatic effects, and provide the ability to predict highly localized concentrations of deposition.

While the SIP model proved effective in the current study and greatly reduced simulation times compared with evaluating the entire TB tree, it remains a complex approach with a number of model selections. Specifically, choices of turbulent and transient flow in the upper TB airways with laminar and steady state flow beginning at B4 were implemented. These assumptions simplified the solution procedure in the SIP geometry and maintained accuracy compared with the *in vivo* data. Polydisperse vs. monodisperse aerosols were considered in the SIP geometry and it was determined that polydisperse aerosols had an effect on regional deposition and improved agreement with the *in vivo* data. This is because the aerosol is selectively filtered as it moves through the bifurcating network with larger particles depositing in the upper branches and smaller particles reaching the more distal regions. Considering comparisons with the *in vivo* data on a regional central vs. peripheral basis, improvements were not observed with the evaluation of all five lung lobes vs. assessing average conditions in the LL lobe. It is important to recognize that the approximation of a single lobe does not imply that deposition is the same in all lobes. Instead, conditions in the LL lobe represent an average of conditions across the five human lung lobes, as previously reported by Longest et al. (23) for standing or sitting adults. In the previous analysis of Longest et al. (23), the SIP modeling approach predicted 5-10 fold differences in deposition among the five human lung lobes. In the current results, the inter-lobe deposition variability was also significant. These findings are consistent with the previous analysis of lobar deposition by Subramaniam et al. (93) as well as recent analyses of animal airway models, which highlight inter-lobe variability in aerosol deposition (94, 95). If more localized deposition patterns or inter-lobe differences in deposition are of interest, then considering multiple lobes along with multiple SIPs in each lobe becomes a necessary step in the modeling process.

The SIP modeling approach and CFD simulations to predict deposition throughout the lungs have been extensively developed in previous parameter analysis studies (23, 40-42) and with comparisons to concurrent *in vitro* data in inhalers (96, 97) and the tracheobronchial airways (22, 47, 48, 87). As a result of this extensive model development effort, methodological changes were not needed in this study to match the *in vivo* data. The current study highlights that improved accuracy can be achieved by considering polydisperse aerosols for the two pharmaceutical inhalers considered, as expected. The only notable change in model selection parameters in the current study from our previous work (23, 40, 41) was the use of laminar flow in the region of B4-B7 as described in the Methods, which improved agreement with the *in vivo* data. While the LRN $k-\omega$ model is capable of simulating transitional and laminar flow domains, particle deposition in predominately laminar flow is better predicted without

the complexities of the turbulence model. This is largely because of interpolation inaccuracies in the near-wall region of turbulent and transitional flow, which are difficult to address with a single set of parameters over the large diameter changes occurring between B4 and B7. Future model development work may be needed to find effective solutions that can accurately predict particle deposition in this region using an efficient transitional or turbulent flow model. However, results of the current study indicate that the laminar assumption is acceptable for matching the regional deposition of interest in the region of B4-B15. As previously established, accurate turbulence modeling is required to capture most pharmaceutical aerosol deposition in the mouth-throat and upper TB airways leading to B4 (21, 41, 80, 86), as implemented in the current study.

Agreement with the *in vivo* data was based on a specific mapping between the 2D gamma scintigraphy lung definitions and individual bifurcation numbers. More detailed illustrations of the 2D gamma scintigraphy lung divisions (98) agree with the current association of the central region extending to approximately B7. However, as shown in Figure 2, this mapping is an approximate average among the five lobes with some pathways having more or fewer bifurcations. A primary advantage of this mapping is that it aligns well with the physiological division of large and small airways *in vivo*. The small airways are typically defined as beginning at B8 and include the remainder of the TB airways and the alveolar region (6, 99). As a result, the I+P region of the gamma scintigraphy scans can be considered to consist of the small airways using the currently defined mapping.

One aspect that is not taken into account in the current mapping is the fraction of the peripheral airways that is captured when imaging the central region *in vivo*. This additional component is due to the 2D projection imaging and an associated peripheral component on the front and back of the central region. Correcting the *in vivo* deposition data for this effect would decrease the measured C deposition and increase the measured I+P deposition. However, the corrections are expected to be small (~10% relative difference) and will not adversely affect overall agreement with the CFD modeling regions. When conducting 2D gamma scintigraphy analysis of *in vivo* data, corrections are made for both attenuation and partial volume effects (50, 85). In performing the 2D image analysis of the CFD data, attempts were not made to reproduce these inherent *in vivo* factors and then correct for them. Including these factors in the 3D CFD data along with analogous corrections in the 2D representations may provide a more consistent comparison with the *in vivo* data and imaging process.

An advantage of the CFD model results compared with the *in vivo* imaging data is the increased resolution of local deposition. For the Novolizer inhaler, only 1.8% of the aerosolized dose was delivered to the TB region extending from B8-B15. Deposition fraction predictions in the SIP models are calculated to account for all bifurcations so this value represents the total dose delivered to the region of B8-B15 for the entire lung. This low delivered dose appears to be a significant shortcoming of DPIs for treating conditions that affect the small airways of the TB region, such as asthma and COPD. The Respimat inhaler is observed to increase dose delivery to the small TB airways by a factor of 5x with a delivery efficiency of 9.2%. This large difference in these two common delivery devices was not apparent from the gamma scintigraphy data but is readily predicted with the CFD model.

This improved delivery efficiency may reflect the lower tiotropium doses that are employed clinically using the Spiriva Respimat SMI compared to the Handihaler DPI.

Limitations of the current model include one SIP geometry or one pathway into each lobe, laminar and steady state simulations into the SIP models, time-constant values of ventilation distribution into each lung lobe instead of time varying values, and simulating only inspiratory and breath-hold conditions without considering exhalation. While these assumptions may affect more local deposition patterns, they appear appropriate for matching the regional *in vivo* data selected for this study. Due to the presence of a breath-hold in the pharmaceutical aerosol experiments, little exhalation of the dose occurred and it was not necessary to consider expiratory flow, which was confirmed with the new alveolar model. Future work includes evaluating the models ability to capture the effects of intersubject variability on deposition. Further verification of the CFD model can be achieved by considering additional flow rates and particle sizes available in the *in vivo* datasets selected. Inclusion of more advanced pressure outlet boundary conditions to capture the dynamic lung structure also needs to be explored (37, 38). Additional model verification can be performed with comparisons to more detailed lung deposition data like that provided by the studies of Fleming et al. (19) and Conway et al. (18) for nebulized aerosols.

Perhaps the largest current model limitation is not including the exhalation phase of the breathing cycle on TB deposition. Based on the presence of a breath-hold, TB deposition during exhalation was not significant with the DPI and SMI inhalers. However, TB deposition during exhalation is likely important for improved comparisons with the Stahlhofen et al. (9) data. In the current simulations of the Stahlhofen et al. (9) data, deposition during exhalation is only considered in the alveolar region based on the correlation implemented, but is not included in the TB airways. The previous results of Longest and Vinchurkar (100) showed that TB deposition during exhalation is different from deposition during inhalation and can result in significant additional aerosol loss. Extension of the SIP modeling approach to approximate deposition during exhalation and the exhaled fraction more accurately is a future challenge.

Conclusions

In conclusion, a whole-lung CFD model was shown to capture regional *in vivo* lung deposition for multiple inhalers, aerosols, and imaging techniques. For a DPI and SMI, relative differences in regional deposition between the *in vivo* data and predictions were 9.9 and 8.5%, respectively. This comparison represents the first time whole-lung CFD modeling predictions have been compared with regional *in vivo* deposition for pharmaceutical inhalers. Compared with previous modeling studies, the CFD simulations provided improved predictions in the extrathoracic and alveolar regions as well as accurate simulations in the TB airways. The CFD model predictions also highlighted very low doses and differences in DPI vs. SMI delivered doses in the small TB airways, which were not available in the imaging analysis and may have important clinical implications for treating respiratory diseases affecting this region, such as asthma and COPD.

Acknowledgements

Katharina Bormann and Xiangyin Wei are acknowledged for their assistance in measuring the initial size of the Novolizer DPI. This study was supported by Award U01 FD004570 from the US FDA and Award R01 HL107333 from the National Heart, Lung, and Blood Institute. The content is solely the responsibility of the authors and does not necessarily represent the official views of the US FDA, the National Heart, Lung, and Blood Institute or the National Institutes of Health.

ABBREVIATIONS

1D	one dimensional
2D	two dimensional
3D	three dimensional
B#	airway bifurcation number
C	central
CFD	computational fluid dynamics
COPD	chronic obstructive pulmonary disease
CT	computed tomography
DF	deposition fraction
DPI	dry powder inhaler
EXP	experimental
FRC	functional residual capacity
HPLC	high performance liquid chromatography
I	intermediate
LL	left lower (lung lobe)
LRN	Low Reynolds Number
LPM	Liters per minute
MDI	metered dose inhaler
MMAD	Mass median aerodynamic diameter
MP	mouthpiece
MT	mouth-throat
NGI	Next Generation Impactor
P	peripheral
PIFR	peak inspiratory flow rate
PSD	Particle size distribution
QD	quick-and-deep
SD	slow-and-deep or standard deviation

SIP	stochastic individual pathway
SMI	softmist inhaler
SPECT	single-photon emission computed tomography
TB	tracheobronchial

REFERENCES

- Patton JS, Byron PR. Inhaling medicines: delivering drugs to the body through the lungs. *Nature Reviews Drug Discovery*. 2007; 6:67–74. [PubMed: 17195033]
- Willson DF, Notter RH. The future of exogenous surfactant therapy. *Respiratory Care*. 2011; 56:1369–1388. [PubMed: 21944686]
- Geller DE. Aerosol antibiotics in cystic fibrosis. *Respiratory Care*. 2009; 54:658–670. [PubMed: 19393109]
- Usmani OS, Biddiscombe MF, Barnes PJ. Regional lung deposition and bronchodilator response as a function of beta(2)-agonist particle size. *American Journal Of Respiratory And Critical Care Medicine*. 2005; 172:1497–1504. [PubMed: 16192448]
- Postma DS, van den Berge M. Small airway dysfunction in asthma and COPD: Consequences for therapy and the future. *Respiratory Drug Delivery Europe 2013*. 2013; 1:1–12.
- Usmani OS, Barnes PJ. Assessing and treating small airways disease in asthma and chronic obstructive pulmonary disease. *Annals of Medicine*. 2012; 44:146–156. [PubMed: 21679101]
- Gelfand EW, Kraft M. The importance and features of the distal airways in children and adults. *J Allergy Clin Immunol*. 2009; 124:S84–87. [PubMed: 19962041]
- Longest PW, Holbrook LT. In silico models of aerosol delivery to the respiratory tract - Development and applications. *Advanced Drug Delivery Reviews*. 2012; 64:296–311. [PubMed: 21640772]
- Stahlhofen W, Rudolf G, James AC. Intercomparison of experimental regional aerosol deposition data. *Journal of Aerosol Medicine*. 1989; 2:285–308.
- Finlay WH, Martin AR. Recent advances in predictive understanding of respiratory tract deposition. *Journal of Aerosol Medicine and Pulmonary Drug Delivery*. 2008; 21:189–205. [PubMed: 18518795]
- Martin AR, Finlay WH. A general, algebraic equation for predicting total respiratory tract deposition of micrometer-sized aerosol particles in humans. *Journal Of Aerosol Science*. 2007; 38:246–253.
- DeHaan WH, Finlay WH. Predicting extrathoracic deposition from dry powder inhalers. *Journal of Aerosol Science*. 2004; 35:309–331.
- Choi J, Kim CS. Mathematical analysis of particle deposition in human lungs: an improved single path transport model. *Inhalation Toxicology*. 2007; 19:925–939. [PubMed: 17849277]
- Asgharian B, Hofmann W, Bergmann R. Particle deposition in a multiple-path model of the human lung. *Aerosol Science and Technology*. 2001; 34:332–339.
- Martonen TB. Analytical model of hygroscopic particle behavior in human airways. *Bulletin of Mathematical Biology*. 1982; 44:425–442. [PubMed: 7104512]
- Koblinger L, Hofmann W. Monte Carlo modeling of aerosol deposition in human lungs. Part I: Simulation of particle transport in a stochastic lung structure. *Journal of Aerosol Science*. 1990; 21:661–674.
- Katz I, Pichelin M, Caillibotte G, Montesantos S, Majoral C, Martonen T, Fleming J, Bennett M, Conway J. Controlled, parametric, individualized, 2D, and 3D imaging measurements of aerosol deposition in the respiratory tract of healthy human subjects: Preliminary comparisons with simulations. *Aerosol Science and Technology*. 2013; 47:714–723.
- Conway J, Fleming J, Majoral C, Katz I, Perchet D, Peebles C, Tossici-Bolt L, Collier L, Caillibotte G, Pichelin M, Sauret-Jackson V, Martonen T, Apiou-Sbirlea G, Muellinger B,

- Kroneberg P, Gleske J, Scheuch G, Texereau J, Martin A, Montesantos S, Bennett M. Controlled, parametric, individualized, 2-D and 3-D imaging measurements of aerosol deposition in the respiratory tract of healthy human subjects for model validation. *Journal Of Aerosol Science*. 2012; 52:1–17.
19. Fleming JS, Epps BP, Conway JH, Martonen TB. Comparison of SPECT aerosol deposition data with a human respiratory tract model. *Journal Of Aerosol Medicine-Deposition Clearance And Effects In The Lung*. 2006; 19:268–278.
 20. Kim CS. Deposition of aerosol particles in human lungs: in vivo measurement and modeling. *Biomarkers*. 2009; 14(S1):54–58. [PubMed: 19604060]
 21. Longest PW, Hindle M, Das Choudhuri S, Xi J. Comparison of ambient and spray aerosol deposition in a standard induction port and more realistic mouth-throat geometry. *Journal of Aerosol Science*. 2008; 39:572–591.
 22. Longest PW, Hindle M. Evaluation of the Respimat Soft Mist inhaler using a concurrent CFD and in vitro approach. *Journal of Aerosol Medicine and Pulmonary Drug Delivery*. 2009; 22:99–112. [PubMed: 18956950]
 23. Longest PW, Tian G, Delvadia R, Hindle M. Development of a stochastic individual path (SIP) model for predicting the deposition of pharmaceutical aerosols: Effects of turbulence, polydisperse aerosol size, and evaluation of multiple lung lobes. *Aerosol Science and Technology*. 2012; 46:1271–1285.
 24. Oldham MJ, Phalen RF, Heistracher T. Computational fluid dynamic predictions and experimental results for particle deposition in an airway model. *Aerosol Science and Technology*. 2000; 32:61–71.
 25. Sznitman J, Sutter R, Altorfer D, Stampanonim M, Rosgen T, Schittny JC. Visualization of respiratory flows from 3D reconstructed alveolar airspaces using X-ray tomographic microscopy. *J Vis*. 2010; 13:337–345.
 26. Xi J, Longest PW. Numerical predictions of submicrometer aerosol deposition in the nasal cavity using a novel drift flux approach. *International Journal Of Heat And Mass Transfer*. 2008; 51:5562–5577.
 27. Golshahi L, Noga ML, Finlay WH. Deposition of inhaled micrometer-sized particles in oropharyngeal airway replicas of children at constant flow rates. *Journal of Aerosol Science*. 2012; 49:21–31.
 28. Xi J, Longest PW, Martonen TB. Effects of the laryngeal jet on nano- and microparticle transport and deposition in an approximate model of the upper tracheobronchial airways. *Journal of Applied Physiology*. 2008; 104:1761–1777. [PubMed: 18388247]
 29. Longest PW, Vinchurkar S, Martonen TB. Transport and deposition of respiratory aerosols in models of childhood asthma. *Journal of Aerosol Science*. 2006; 37:1234–1257.
 30. Sznitman J, Heimshch T, Wildhaber JH, Tsuda A, Rosgen T. Respiratory flow phenomena and gravitational deposition in a three-dimensional space-filling model of the pulmonary acinar tree. *Journal of Biomechanical Engineering*. 2009; 131:031010–031011-031015. [PubMed: 19154069]
 31. Lambert AR, O'Shaughnessy PT, Tawhai MH, Hoffman EA, Lin C-L. Regional deposition of particles in an image-based airway model: Large-eddy simulation and left-right lung ventilation asymmetry. *Aerosol Science and Technology*. 2011; 45:11–25. [PubMed: 21307962]
 32. Inthavong K, Choi L-T, Tu J, Diang S, Thien F. Micron particle deposition in a tracheobronchial airway model under different breathing conditions. *Medical Engineering and Physics*. 2010; 32:1198–1212. [PubMed: 20855226]
 33. Lin C-L, Tawhai MH, McLennan G, Hoffman EA. Characteristics of the turbulent laryngeal jet and its effect on airflow in the human intra-thoracic airways. *Respiratory Physiology and Neurobiology*. 2007; 157:295–309. [PubMed: 17360247]
 34. Choi J, Tawhai M, Hoffman EA, Lin CL. On intra- and intersubject variabilities of airflow in the human lungs. *Physics of Fluids*. 2009; 21:101901–101901-101917. [PubMed: 19901999]
 35. Li Z, Kleinstreuer C, Zhang Z. Particle deposition in the human tracheobronchial airways due to transient inspiratory flow patterns. *Aerosol Science*. 2007; 38:625–644.
 36. Lin C-L, Tawhai MH, McLennan G, Hoffman EA. Multiscale simulation of gas flow in subject-specific models of the human lung. *IEEE Engineering in Medicine and Biology*. 2009; 28:25–33.

37. Walters DK, Luke WH. A method for three-dimensional Navier Stokes simulations of large-scale regions of the human lung airway. *Journal of Fluids Engineering*. 2010;051101.
38. Walters DK, Luke WH. Computational fluid dynamics simulations of particle deposition in large-scale multigenerational lung models. *Journal of Biomechanical Engineering*. 2011; 133:011003. [PubMed: 21186893]
39. Kleinstreuer C, Zhang Z. An adjustable triple-bifurcation unit model for air-particle flow simulations in human tracheobronchial airways. *Journal of Biomechanical Engineering*. 2009; 131:021007. [PubMed: 19102566]
40. Tian G, Longest PW, Su G, Walenga RL, Hindle M. Development of a stochastic individual path (SIP) model for predicting the tracheobronchial deposition of pharmaceutical aerosols: Effects of transient inhalation and sampling the airways. *Journal of Aerosol Science*. 2011; 42:781–799.
41. Longest PW, Tian G, Walenga RL, Hindle M. Comparing MDI and DPI aerosol deposition using in vitro experiments and a new stochastic individual path (SIP) model of the conducting airways. *Pharmaceutical Research*. 2012; 29:1670–1688. [PubMed: 22290350]
42. Khajeh-Hosseini-Dalasm N, Longest PW. Deposition of particles in the alveolar airways: Inhalation and breath-hold with pharmaceutical aerosols. *Journal of Aerosol Science*. 2015; 79:15–30. [PubMed: 25382867]
43. Tian G, Longest PW, Su G, Hindle M. Characterization of respiratory drug delivery with enhanced condensational growth (ECG) using an individual path model of the entire tracheobronchial airways. *Annals of Biomedical Engineering*. 2011; 39:1136–1153. [PubMed: 21152983]
44. Tian G, Longest PW, Li X, Hindle M. Targeting aerosol deposition to and within the lung airways using excipient enhanced growth. *Journal of Aerosol Medicine and Pulmonary Drug Delivery*. 2013; 26:248–265. [PubMed: 23286828]
45. Tian G, Hindle M, Longest PW. Targeted lung delivery of nasally administered aerosols. *Aerosol Science and Technology*. 2014; 48:434–449. [PubMed: 24932058]
46. Longest PW, Tian G, Li X, Son Y-J, Hindle M. Performance of combination drug and hygroscopic excipient submicrometer particles from a softmist inhaler in a characteristic model of the airways. *Annals of Biomedical Engineering*. 2012; 40:2596–2610. [PubMed: 22820981]
47. Longest PW, Vinchurkar S. Validating CFD predictions of respiratory aerosol deposition: effects of upstream transition and turbulence. *Journal of Biomechanics*. 2007; 40:305–316. [PubMed: 16533511]
48. Holbrook LT, Longest PW. Validating CFD predictions of highly localized aerosol deposition in airway models: In vitro data and effects of surface properties. *Journal of Aerosol Science*. 2013; 59:6–21.
49. Longest PW, Oldham MJ. Mutual enhancements of CFD modeling and experimental data: A case study of one micrometer particle deposition in a branching airway model. *Inhalation Toxicology*. 2006; 18:761–772. [PubMed: 16774865]
50. Biddiscombe MF, Meah SN, Underwood SR, Usmani OS. Comparing lung regions of interest in gamma scintigraphy for assessing inhaled therapeutic aerosol deposition. *Journal Of Aerosol Medicine And Pulmonary Drug Delivery*. 2011; 24:165–173. [PubMed: 21453048]
51. Newman SP, Pitcairn GR, Hirst PH, Bacon RE, O'Keefe E, Reiners M, Hermann R. Scintigraphic comparison of budesonide deposition from two dry powder inhalers. *European Respiratory Journal*. 2000; 16:178–183. [PubMed: 10933104]
52. Newman SP, Brown J, Steed KP, Reader SJ, Kladders H. Lung deposition of fenoterol and flunisolide delivered using a novel device for inhaled medicines. *Chest*. 1998; 113:957–963. [PubMed: 9554631]
53. Walenga RL, Tian G, Longest PW. Development of characteristic upper tracheobronchial airway models for testing pharmaceutical aerosol delivery. *ASME Journal of Biomechanical Engineering*. 2013; 135(9):091010.
54. Delvadia R, Longest PW, Byron PR. In vitro tests for aerosol deposition. I. Scaling a physical model of the upper airways to predict drug deposition variation in normal humans. *Journal of Aerosol Medicine*. 2012; 25:32–40.
55. Asgharian B, Hofmann W, Miller FJ. Mucociliary clearance of insoluble particles from the tracheobronchial airways of the human lung. *J. Aerosol Science*. 2001; 32:817–832.

56. Heyder J, Gebhart J, Rudolf G, Schiller CF, Stahlhofen W. Deposition of particles in the human respiratory tract in the size range of 0.005 - 15 microns. *Journal of Aerosol Science*. 1986; 17:811–825.
57. Newman SP, Clark SR, Talaei N, Clarke SW. Pressurised aerosol deposition in the human lung with and without an open spacer. *Thorax*. 1989;44.
58. Steed KP, Towse LJ, Freund B, Newman SP. Lung and oropharyngeal depositions of fenoterol hydrobromide delivered from the prototype III hand-held multidose Respimat nebuliser. *Eur. J. Pharm. Sci*. 1997; 5:55–61.
59. Delvadia RR, Longest PW, Hindle M, Byron PR. In Vitro Tests for Aerosol Deposition. III: Effect of Inhaler insertion angle on aerosol deposition. *Journal of Aerosol Medicine and Pulmonary Drug Delivery*. 2013; 26:145–156. [PubMed: 23025452]
60. Fenton C, Keating GM, Plosker GL. Novolizer: A multidose dry powder inhaler. *Drugs*. 2003; 63:2437–2445. [PubMed: 14609355]
61. Dalby R, Spallek M, Voshaar T. A review of the development of Respimat soft mist inhaler. *International Journal of Pharmaceutics*. 2004; 283:1–9. [PubMed: 15363496]
62. Hochrainer D, Holz H, Kreher C, Scaffidi L, Spallek M, Wachtel H. Comparison of the aerosol velocity and spray duration of Respimat soft mist inhaler and pressurized metered dose inhalers. *Journal of Aerosol Medicine*. 2005; 18:273–282. [PubMed: 16181002]
63. Longest, PW.; Hindle, M.; Das Choudhuri, S.; Byron, PR. Developing a better understanding of spray system design using a combination of CFD modeling and experiment.. In: Dalby, RN.; Byron, PR.; Peart, J.; Suman, JD.; Farr, SJ.; Young, PM., editors. *Proceedings of Respiratory Drug Delivery 2008*. Davis Healthcare International Publishing; Illinois: 2008.
64. Pitcairn G, Reader S, Pavia D, Newman S. Deposition of corticosteroid aerosol in the human lung by Respimat Soft Mist inhaler compared to deposition by metered dose inhaler or by Turbuhaler dry power inhaler. *Journal of Aerosol Medicine*. 2005; 18:264–272. [PubMed: 16181001]
65. Xi J, Longest PW. Transport and deposition of micro-aerosols in realistic and simplified models of the oral airway. *Annals of Biomedical Engineering*. 2007; 35:560–581. [PubMed: 17237991]
66. Cheng KH, Cheng YS, Yeh HC, Swift DL. Measurements of airway dimensions and calculation of mass transfer characteristics of the human oral passage. *Journal of Biomechanical Engineering*. 1997; 119:476–482. [PubMed: 9407288]
67. Delvadia R, Hindle M, Longest PW, Byron PR. In vitro tests for aerosol deposition II: IVIVCs for different dry powder inhalers in normal adults. *Journal of Aerosol Medicine and Pulmonary Drug Delivery*. 2013; 26:138–144. [PubMed: 22947131]
68. Yeh HC, Schum GM. Models of human lung airways and their application to inhaled particle deposition. *Bull. Math. Biology*. 1980; 42:461–480.
69. ICRP. *Human Respiratory Tract Model for Radiological Protection*. Elsevier Science Ltd.; New York: 1994.
70. Fleming JS, Sauret V, Conway JH, Martonen TB. Validation of the conceptual anatomical model of the lung airway. *Journal of Aerosol Medicine-Deposition Clearance and Effects in the Lung*. 2004; 17:260–269.
71. Heistracher T, Hofmann W. Physiologically realistic models of bronchial airway bifurcations. *Journal of Aerosol Science*. 1995; 26:497–509.
72. Vinchurkar S, Longest PW. Evaluation of hexahedral, prismatic and hybrid mesh styles for simulating respiratory aerosol dynamics. *Computers and Fluids*. 2008; 37:317–331.
73. Phalen RF, Yeh HC, Schum GM, Raabe OG. Application of an idealized model to morphometry of the mammalian tracheobronchial tree. *Anat. Rec*. 1978; 190:167–176. [PubMed: 629400]
74. Ghalichi F, Deng X, Champlain AD, Douville Y, King M, Guidoin R. Low Reynolds number turbulence modeling of blood flow in arterial stenoses. *Biorheology*. 1998; 35:281–294. [PubMed: 10474655]
75. Wilcox, DC. *Turbulence Modeling for CFD*. 2nd Ed.. DCW Industries, Inc.; California: 1998.
76. Longest PW, Xi J. Condensational growth may contribute to the enhanced deposition of cigarette smoke particles in the upper respiratory tract. *Aerosol Science and Technology*. 2008; 42:579–602.

77. Longest PW, Kleinstreuer C, Buchanan JR. Efficient computation of micro-particle dynamics including wall effects. *Computers & Fluids*. 2004; 33:577–601.
78. Longest PW, Xi J. Effectiveness of direct Lagrangian tracking models for simulating nanoparticle deposition in the upper airways. *Aerosol Science and Technology*. 2007; 41:380–397.
79. Gosman AD, Ioannides E. Aspects of computer simulation of liquid-fueled combustors. *Journal of Energy*. 1981; 7:482–490.
80. Matida EA, Finlay WH, Grgic LB. Improved numerical simulation of aerosol deposition in an idealized mouth-throat. *Journal of Aerosol Science*. 2004; 35:1–19.
81. Wang Y, James PW. On the effect of anisotropy on the turbulent dispersion and deposition of small particles. *International Journal of Multiphase Flow*. 1999; 22:551–558.
82. Horsfield K, Dart G, Olson DE, Filley GF, Cumming G. Models of the human bronchial tree. *Journal of Applied Physiology*. 1971; 31:207–217. [PubMed: 5558242]
83. Asgharian B, Price OT. Airflow distribution in the human lung and its influence on particle deposition. *Inhalation Toxicology*. 2006; 18:795–801. [PubMed: 16774869]
84. Yin Y, Choi J, Hoffman EA, Tawhai MH, Lin C-L. Simulation of pulmonary air flow with a subject-specific boundary condition. *Journal of Biomechanics*. 2010; 43:2159–2163. [PubMed: 20483412]
85. Newman S, Bennett WD, Biddiscombe M, Devadason SG, Dolovich MB, Fleming J, Haeussermann S, Kietzig C, Kuehl PJ, Laube BL, Sommerer K, Taylor G, Usmani OS, Zeman KL. Standardization of techniques for using planar (2D) imaging for aerosol deposition assessment of orally inhaled products. *Journal of Aerosol Medicine and Pulmonary Drug Delivery*. 2012; 25:S10–S28. [PubMed: 23215844]
86. Matida EA, Finlay WH, Breuer M, Lange CF. Improving prediction of aerosol deposition in an idealized mouth using large-eddy simulation. *Journal of Aerosol Medicine*. 2006; 19:290–300. [PubMed: 17034305]
87. Longest PW, Hindle M, Das Choudhuri S, Byron PR. Numerical simulations of capillary aerosol generation: CFD model development and comparisons with experimental data. *Aerosol Science and Technology*. 2007; 41:952–973.
88. Kleinstreuer C, Shi H, Zhang Z. Computational analyses of a pressurized metered dose inhaler and an new drug-aerosol targeting methodology. *Journal of Aerosol Medicine*. 2007; 20:294–309. [PubMed: 17894536]
89. Vinchurkar S, De Backer L, Vos WG, Van Holsbeke C, De Backer J, De Backer W. A case series on lung deposition analysis of inhaled medication using functional imaging based computational fluid dynamics in asthmatic patients: effect of upper airway morphology and comparison with in vivo data. *Inhalation Toxicology*. 2012; 24:81–88. [PubMed: 22260527]
90. Chan TL, Lippmann M. Experimental measurements and empirical modeling of the regional deposition of inhaled particles in humans. *American Industrial Hygiene Association Journal*. 1980; 41:399–409. [PubMed: 7395753]
91. Hofmann W, Koblinger L. Monte-Carlo Modeling Of Aerosol Deposition In Human Lungs .3. Comparison With Experimental-Data. *Journal Of Aerosol Science*. 1992; 23:51–63.
92. Longest PW, Hindle M. Condensational growth of combination drug-excipient submicrometer particles: Comparison of CFD predictions with experimental results. *Pharmaceutical Research*. 2012; 29:707–721. [PubMed: 21948458]
93. Subramaniam RP, Asgharian B, Freijer JI, Miller FJ, Anjilvel S. Analysis of lobar differences in particle deposition in the human lung. *Inhalation Toxicology*. 2003; 15:1–21. [PubMed: 12476357]
94. Oakes JM, Marsden AL, Grandmont C, Darquenne C, Vignon-Clementel IE. Distribution of aerosolized particles in healthy and emphysematous rat lungs: Comparison between experimental and numerical studies. *Journal of Biomechanics*. 2015 in press.
95. Oakes JM, Scadeng M, Breen EC, Prisk GK, Darquenne C. Regional distribution of aerosol deposition in rat lungs using magnetic resonance imaging. *Annals of Biomedical Engineering*. 2013; 41:967–978. [PubMed: 23354670]

96. Longest PW, Hindle M. Quantitative analysis and design of a spray aerosol inhaler. Part 1: Effects of dilution air inlets and flow paths. *Journal of Aerosol Medicine and Pulmonary Drug Delivery*. 2009; 22:271–283. [PubMed: 19466904]
97. Hindle M, Longest PW. Quantitative analysis and design of a spray aerosol inhaler. Part 2: Improvements in mouthpiece performance. *Journal of Aerosol Medicine and Pulmonary Drug Delivery*. 2013; 26:237–247. [PubMed: 23098326]
98. Newman SP, Pitcairn GR, Hirst RH, Rankin L. Radionuclide imaging technologies and their use in evaluating asthma drug deposition in the lungs. *Advanced Drug Delivery Reviews*. 2003; 55:851–867. [PubMed: 12842604]
99. Weibel, ER. *Morphometry of the Human Lung*. Springer Verlag; Berlin: 1963.
100. Longest PW, Vinchurkar S. Inertial deposition of aerosols in bifurcating models during steady expiratory flow. *Journal of Aerosol Science*. 2009; 40:370–378.

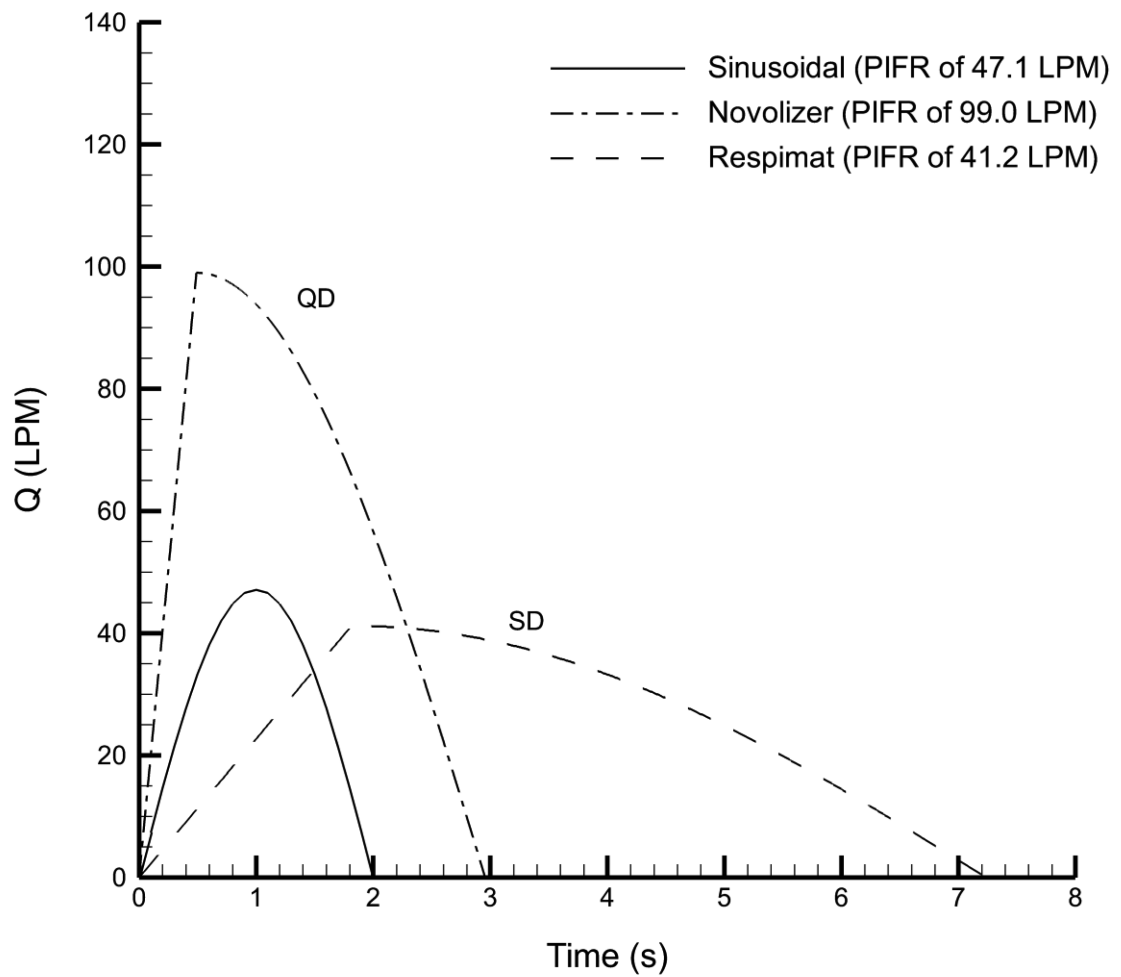


Figure 1. Inhalation waveforms consistent with the selected *in vivo* datasets. The waveform used with the Novolizer DPI is characterized as “quick and deep” (QD) inhalation and the waveform used with the Respimat SMI is characterized as “slow and deep” (SD) inhalation.

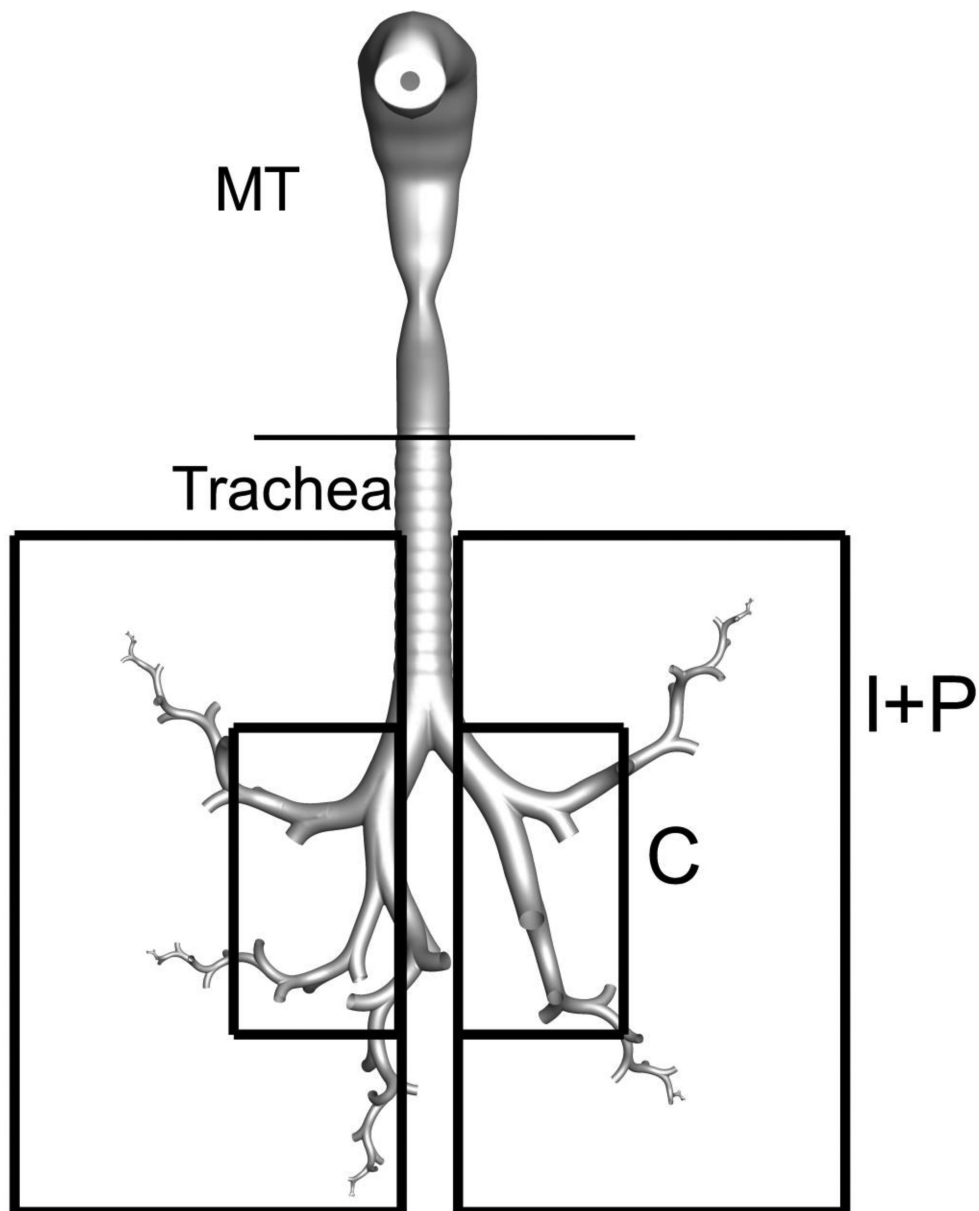


Figure 2. Complete conducting airway model with the Novolizer mouthpiece inserted into the mouth-throat (MT). The airways include all branches through B3 (approximate lobar bronchi). One stochastic individual pathway (SIP) model is illustrated entering each of the five lung lobes. The rectangles indicate expected mappings to 2D gamma scintigraphy images with an outer region capturing the intermediate (I) and peripheral (P) airways and a 20% area inner region capturing the central (C) airways.

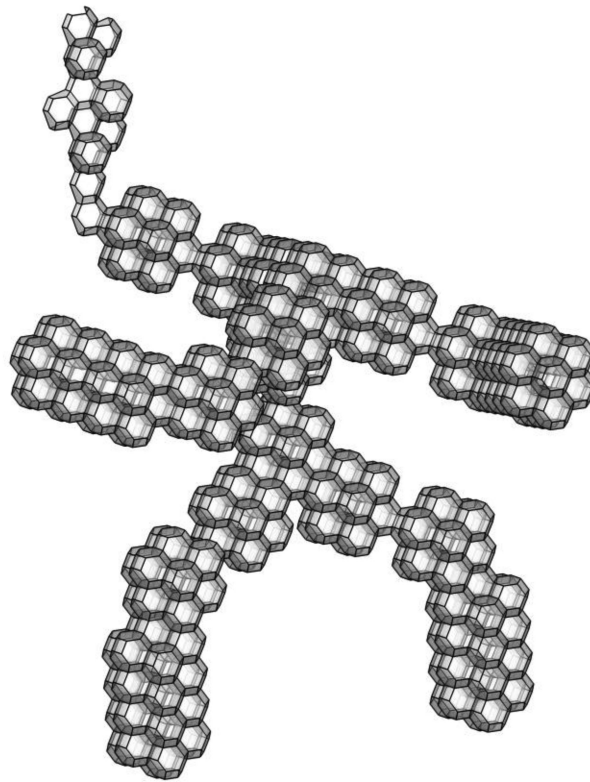


Figure 3. Surface model of the alveolar geometry using a space filling approach designed to capture deposition in a complete acinar region distal to a terminal bronchiole and beginning with a respiratory bronchiole.

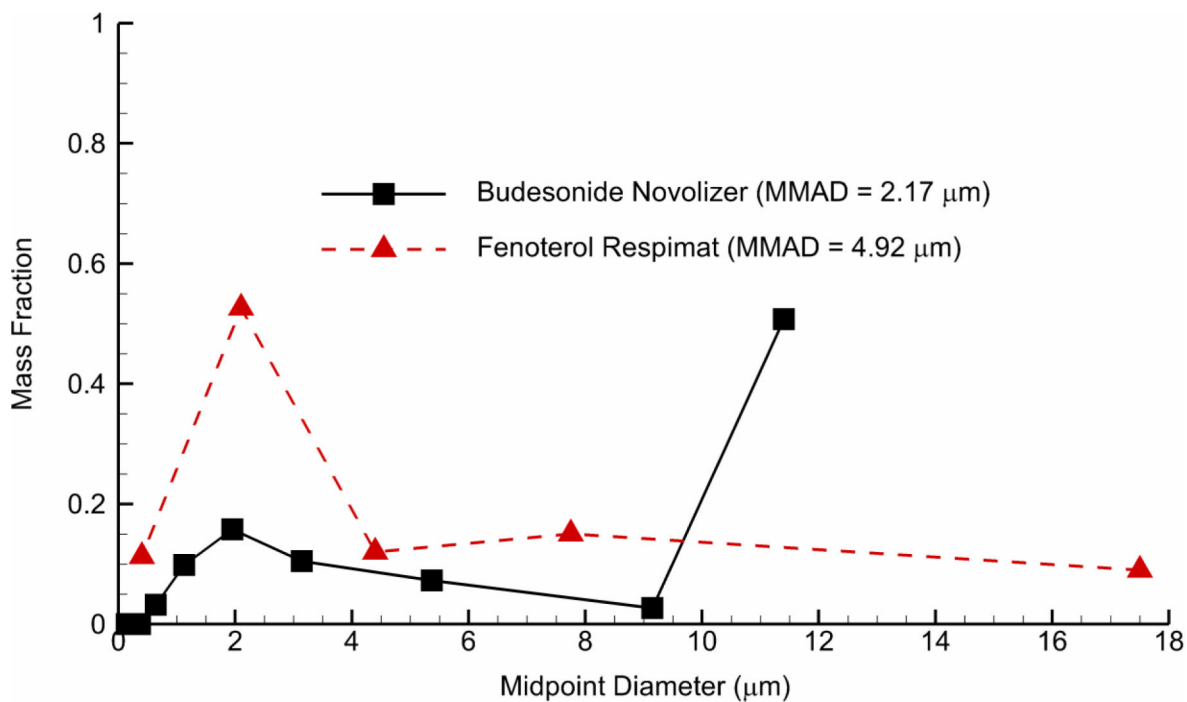


Figure 4. Mass fraction of the particle size distribution (PSD) produced by the Novolizer DPI and Respimat SMI inhalers. Values for the Respimat PSD were reported in the study of Steed et al. (58), whereas new values for the Novolizer at a constant flow rate of 80 LPM were measured in this study.

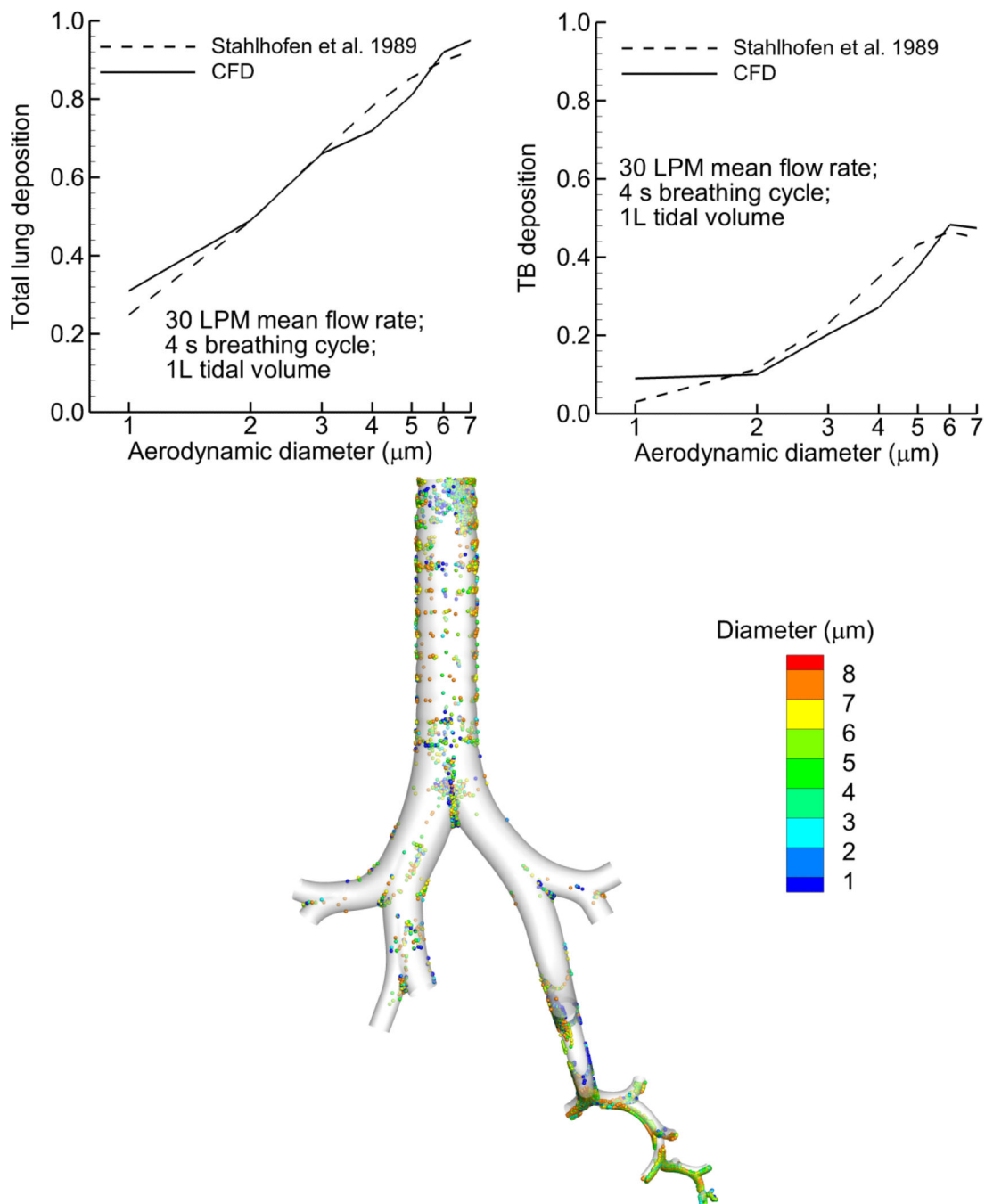


Figure 5. Comparison of CFD estimates to monodisperse particle deposition *in vivo* data reported by Stahlhofen et al. (9). Breathing conditions were a tidal volume of 1 L, 2 s inhalation (4 s breathing cycle) resulting in a mean 30 LPM inhalation flow rate with a sinusoidal waveform. Results are presented in terms of total lung deposition fraction, TB deposition fraction, and a localized deposition map for all particle sizes considered.

Novolizer (PIFR=99 LPM)

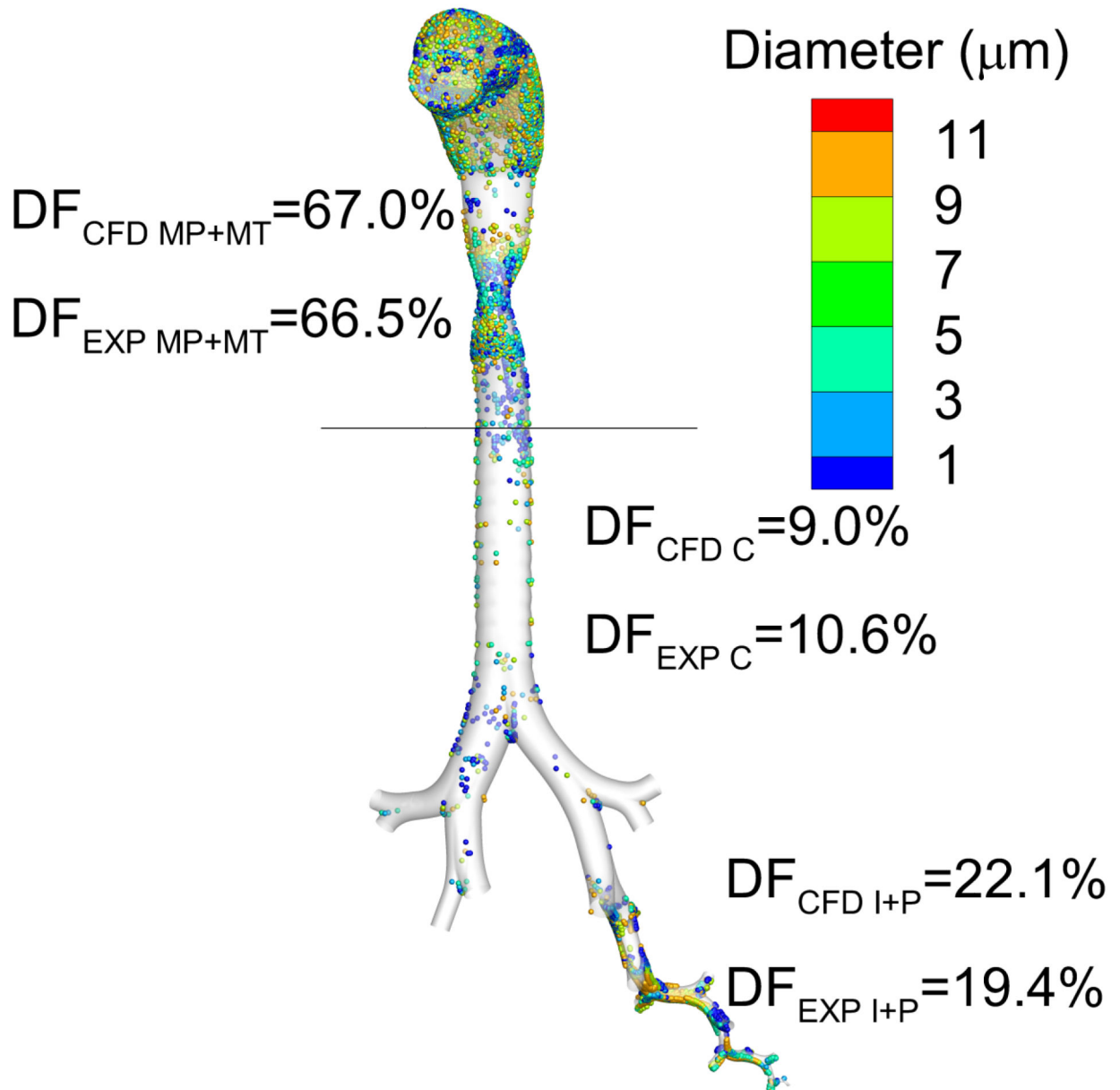


Figure 6. Comparison of *in vivo* and CFD predictions of deposition fraction (DF) in different regions of the airways for the Novolizer DPI with a budesonide formulation. Using the single left lower (LL) lobe estimate, agreement is observed between the *in vivo* data and model predictions.

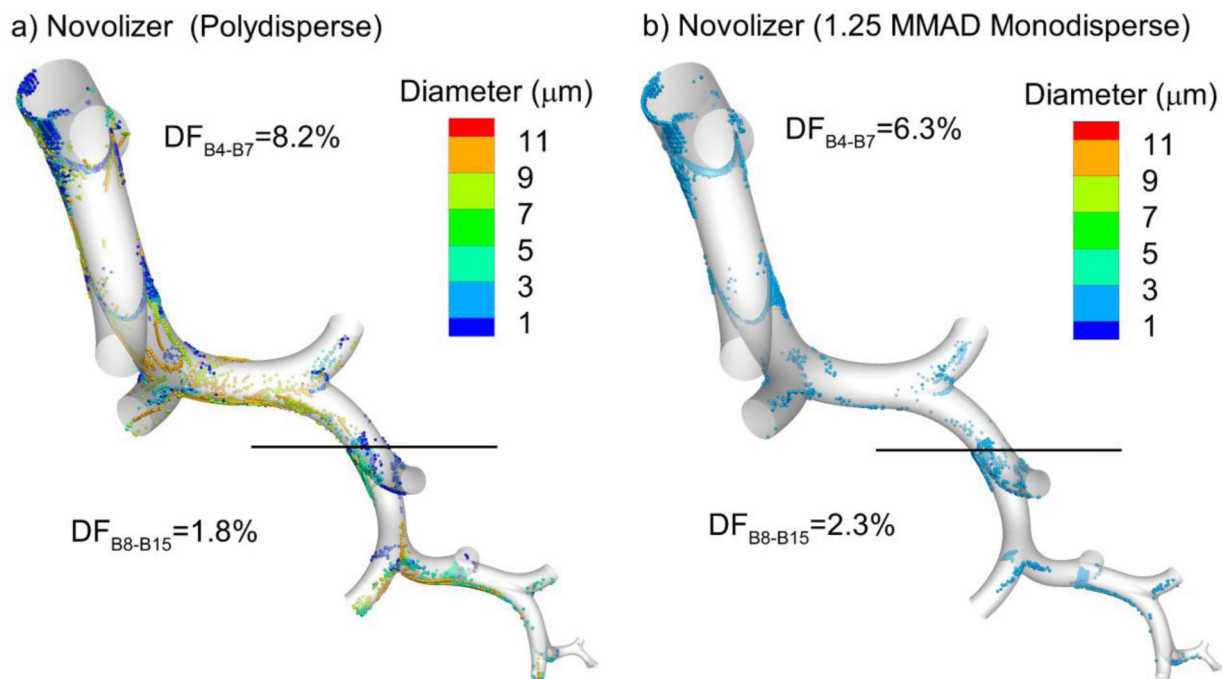


Figure 7. Regional deposition fraction (DF) predictions for the Novolizer in B4-B7 and B8-B15 implementing (a) the more accurate polydisperse simulation vs. (b) the monodisperse approximation. Implementing the correction factor of $1.25 \times \text{MMAD}$ cannot fully account for deposition of the polydisperse aerosol in these two different lung regions. However, the combined DF in B4-B15 for the polydisperse aerosol (10%) is reasonably close to the monodisperse estimate (8.6%).

Respimat (PIFR=41 LPM)

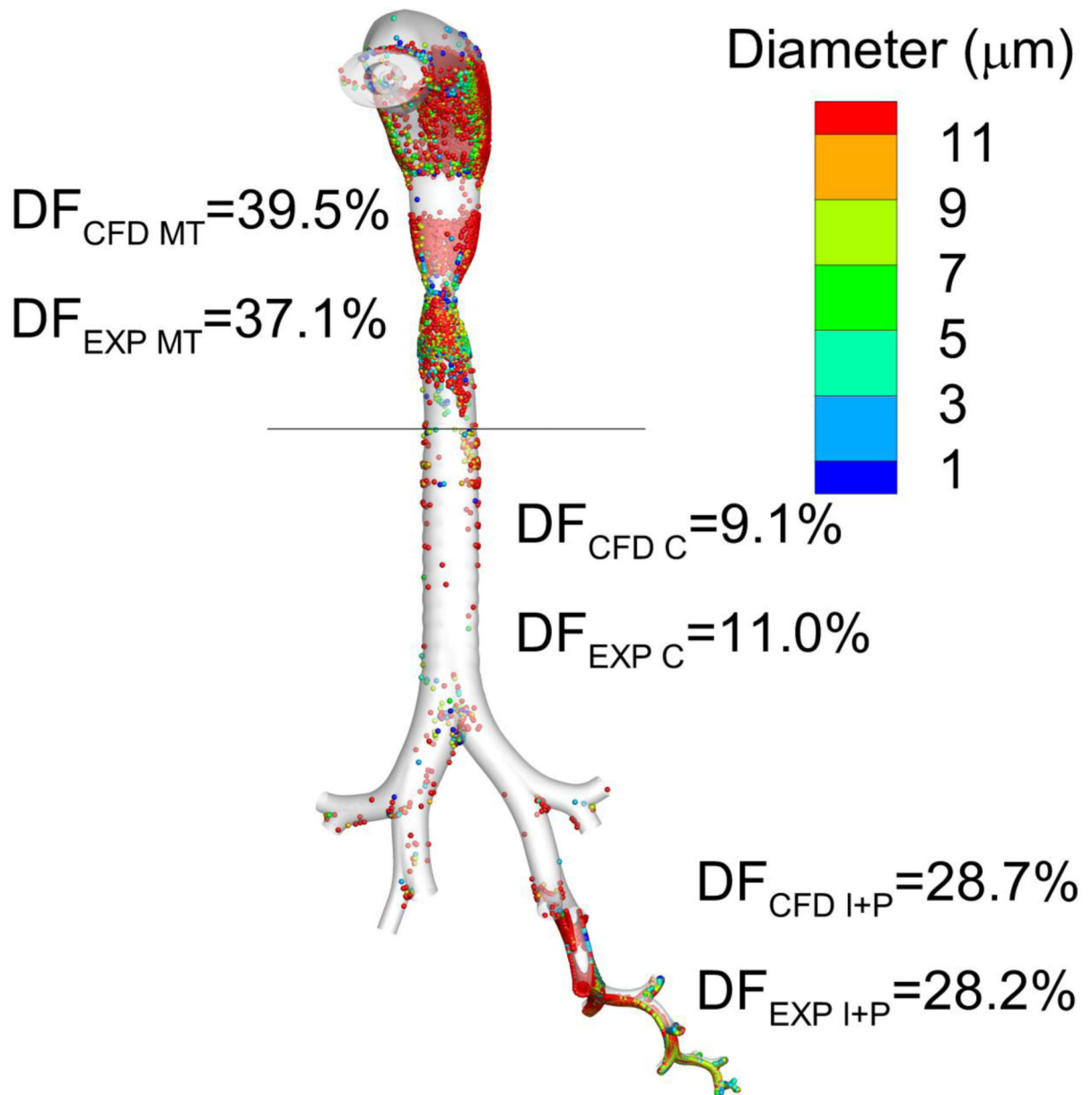


Figure 8. Comparison of *in vivo* and CFD predictions of deposition fraction (DF) in different regions of the airways for the Respimat inhaler with a fenoterol formulation. Using the single left lower (LL) lobe estimate, agreement is observed between the *in vivo* data and model predictions.

Respimat (PIFR=41 LPM)

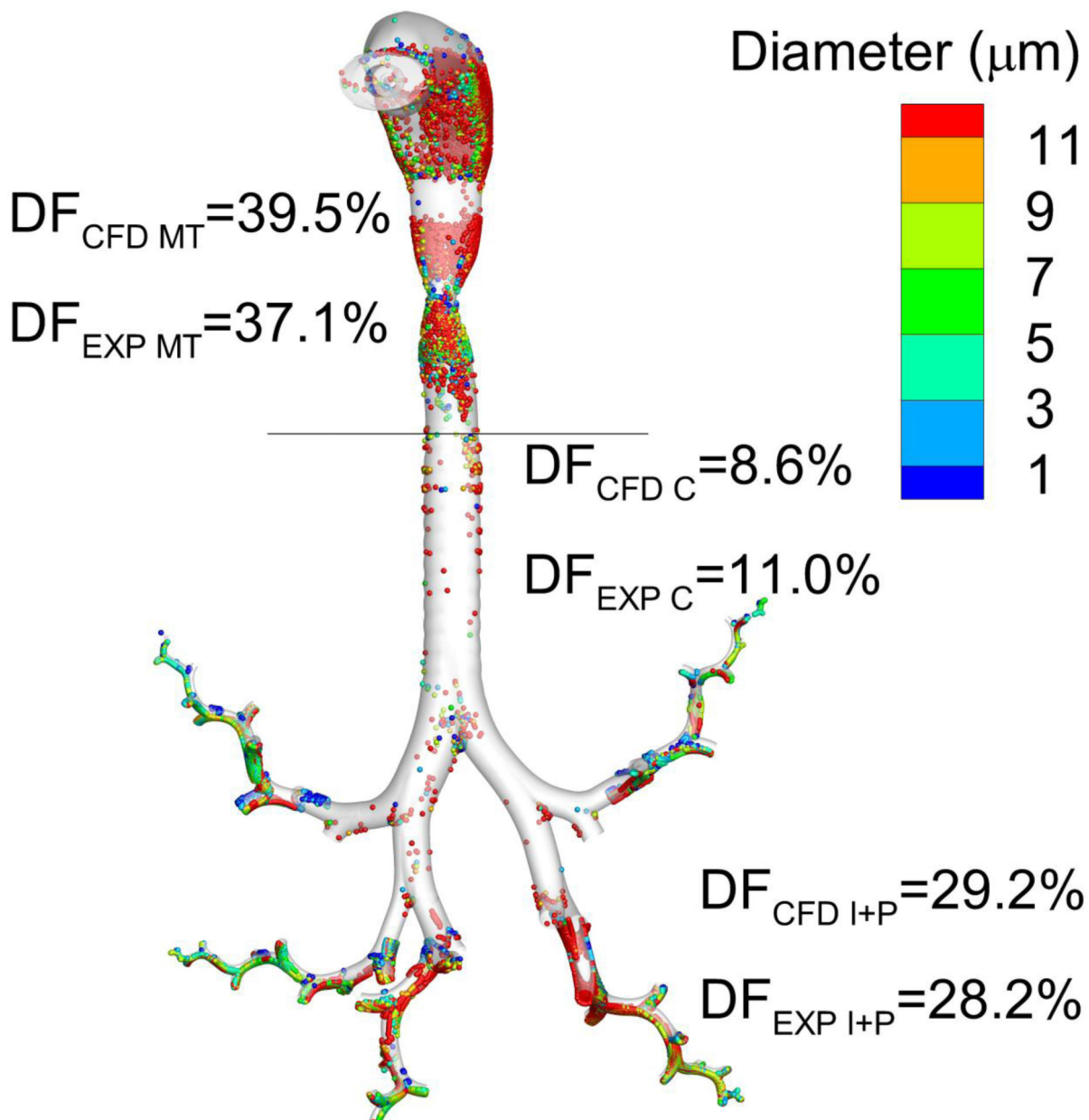


Figure 9.

Comparison of *in vivo* and CFD predictions of DF in different regions of the airways for the Respimat inhaler with a fenoterol formulation considering one SIP geometry in each lung lobe. As with the LL lobe approximation, agreement is again achieved between the *in vivo* data and model predictions by considering one SIP geometry extending into each lung lobe.

Table 1

Characteristics of the flow waveforms used for comparisons to multiple *in vivo* data sets.

	Sinusoidal waveform	QD waveform	SD waveform
PIFR (LPM)	47.1	99.0	41.2
Mean flow rate (LPM)	30.0	60.8	24.8
Flow rate for particle sizing (LPM)	NA	80.0	39.9
Period of inhalation (s)	2	2.96	7.24
Time to PIFR (s)	1	0.49	1.81
Time fraction to PIFR	1/2	1/6	1/4
Volume inhaled (L)	1	3	3

Author Manuscript

Author Manuscript

Author Manuscript

Author Manuscript

Table 2

Deposition fractions (based on particles entering the MT) predicted with CFD compared with the *in vivo* data of Stahlhofen et al. (9) (in parentheses) for the sinusoidal inhalation waveform.

Particle diameter (μm)	Total Lung Deposition	TB Deposition
1	0.31 (0.25)	0.09 (0.03)
2	0.49 (0.49)	0.1 (0.11)
3	0.66 (0.66)	0.2 (0.23)
4	0.72 (0.78)	0.27 (0.35)
5	0.81 (0.85)	0.37 (0.43)
6	0.92 (0.90)	0.48 (0.46)
7	0.95 (0.92)	0.47 (0.45)

Author Manuscript

Author Manuscript

Author Manuscript

Author Manuscript

Table 3

Deposition fractions (as a percentage of aerosolized dose) based on CFD predictions compared with the *in vivo* data of Newman et al. (51) (in parentheses) for the Novolizer operated with a QD waveform and PIFR of 99 LPM.

MP+MT	67 (66.5)
Central lung (trachea excluded)	9.0 (10.6)
Intermediate and peripheral lung	22.1 (19.4)
Trachea-B3	2.7
B4-B7	8.2
B8-B15	1.8
Alveolar	20.3

Table 4

Deposition fractions (as a percentage of aerosolized dose) based on CFD predictions compared with the *in vivo* data of Newman et al. (52) (in parentheses) for the Respimat SMI operated with a SD waveform and PIFR of 41.2 LPM.

Device	NA (21.9)
MT	39.5 (37.1)
Central lung (trachea excluded)	9.1 (11.0)
Intermediate and peripheral lung	28.7 (28.2)
Trachea-B3	1.0
B4-B7	8.9
B8-B15	9.2
Alveolar	19.5